Cell Reports

Article

FER regulates endosomal recycling and is a predictor for adjuvant taxane benefit in breast cancer

Graphical abstract

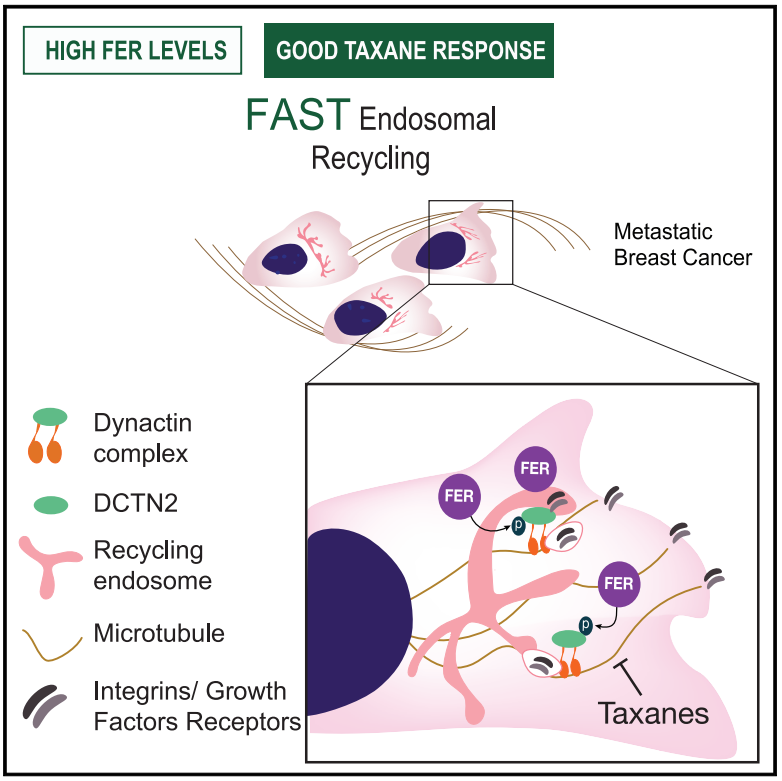

Authors

Sandra Tavares, Nalan Liv, Milena Pasolli, ..., Judith Klumperman, Sabine C. Linn, Patrick W.B. Derksen

Correspondence

p.w.b.derksen@umcutrecht.nl

In brief

Clinical management of triple-negative breast cancer requires the identification of new predictive and targetable biomarkers. Here, Tavares et al. demonstrate that the feline sarcoma-related non-receptor tyrosine kinase FER controls invasion-propagating endosomal recycling and that high FER expression is a candidate predictive marker for taxane-containing adjuvant-chemotherapy benefit in high-risk breast cancer.

Highlights

- Chemical genetics identify DCTN2-Tyr6 as an FER substrate
- FER regulates endosomal recycling to control breast cancer cell invasion
- DCTN2 is necessary for breast cancer cell invasion in 3D
- FER predicts better outcome for taxane-based therapy in high-risk breast cancer

Tavares et al., 2022, Cell Reports *39*, 110584
April 5, 2022
https://doi.org/10.1016/j.celrep.2022.110584

CellPress

Cell Reports

CellPress
OPEN ACCESS

Article

FER regulates endosomal recycling and is a predictor for adjuvant taxane benefit in breast cancer

Sandra Tavares,[1] Nalan Liv,[2] Milena Pasolli,[3] Mark Opdam,[4] Max A.K. Rätze,[1] Manuel Saornil,[1] Lilian M. Sluimer,[1] Rutger C.C. Hengeveld,[6] Robert van Es,[6] Erik van Werkhoven,[4] Harmjan Vos,[6] Holger Rehmann,[7] Boudewijn M.T. Burgering,[6] Hendrika M. Oosterkamp,[8] Susanne M.A. Lens,[6] Judith Klumperman,[2] Sabine C. Linn,[1,4,5] and Patrick W.B. Derksen[1,9,*]

[1]Department of Pathology, University Medical Center Utrecht, 3584CX Utrecht, the Netherlands
[2]Section Cell Biology, Center for Molecular Medicine, University Medical Center Utrecht, 3584CX Utrecht, the Netherlands
[3]Cell Biology, Neurobiology, and Biophysics, Department of Biology, Faculty of Science, Utrecht University, 3584CH Utrecht, the Netherlands
[4]Department of Molecular Pathology, Netherlands Cancer Institute, 1066CX Amsterdam, the Netherlands
[5]Department of Medical Oncology, Netherlands Cancer Institute, 1066CX Amsterdam, the Netherlands
[6]Oncode Institute, Department of Molecular Cancer Research, University Medical Center Utrecht, 3584CX Utrecht, the Netherlands
[7]Flensburg University of Applied Sciences, 24943 Flensburg, Germany
[8]Department of Medical Oncology, Haaglanden Medisch Centrum, 2501 CK The Hague, the Netherlands
[9]Lead contact
*Correspondence: p.w.b.derksen@umcutrecht.nl
https://doi.org/10.1016/j.celrep.2022.110584

SUMMARY

Elevated expression of non-receptor tyrosine kinase FER is an independent prognosticator that correlates with poor survival of high-grade and basal/triple-negative breast cancer (TNBC) patients. Here, we show that high FER levels are also associated with improved outcomes after adjuvant taxane-based combination chemotherapy in high-risk, HER2-negative patients. In TNBC cells, we observe a causal relation between high FER levels and sensitivity to taxanes. Proteomics and mechanistic studies demonstrate that FER regulates endosomal recycling, a microtubule-dependent process that underpins breast cancer cell invasion. Using chemical genetics, we identify DCTN2 as a FER substrate. Our work indicates that the DCTN2 tyrosine 6 is essential for the development of tubular recycling domains in early endosomes and subsequent propagation of TNBC cell invasion in 3D. In conclusion, we show that high FER expression promotes endosomal recycling and represents a candidate predictive marker for the benefit of adjuvant taxane-containing chemotherapy in high-risk patients, including TNBC patients.

INTRODUCTION

Currently, chemotherapy is a major systemic treatment option for invasive breast cancer (Cardoso et al., 2020). Although the overall survival in breast cancer has significantly improved over the past decades, treatment outcomes for high-risk breast cancer patients can still be significantly improved (Thomas and Gustafsson, 2011). One high-risk breast cancer subtype concerns triple-negative breast cancer (TNBC). Due to the metastatic potential of TNBC and lack of targeted therapy options, further molecular insight is needed to identify specific and pharmacologically relevant targets for disease management, especially for this subtype.

A strong candidate for targeted intervention is the feline sarcoma-related non-receptor tyrosine kinase FER. High expression of FER has been linked to tumor progression in several cancer types (Ahn et al., 2013; Li et al., 2009; Zirngibl et al., 2001). In breast cancer, high FER expression is an independent predictor of decreased patient survival, especially in lymph-node-negative TNBC (Ivanova et al., 2013). FER belongs to a distinct subfamily that shares a common structure, consisting of an FES/FER/CIP4 homology (FCH) domain, followed by three regions of predicted coiled-coil domains, a central SH2 domain, and a carboxy-terminal kinase domain (Greer, 2002). The FCH domain is adjacent to a coiled-coil region similar to the one present in the membrane-interacting BAR domain proteins (Bin1, Amphiphysin, and Rsv) (Chen et al., 2013). Together, they constitute a functional unit that is termed as the F-BAR domain and that has been linked to regulation of a plethora of cellular processes such as endocytosis (e.g., CIP4), phagocytosis (e.g., FBP17), cytokinesis (e.g., PSTPIP1), and adhesion (e.g., FER, PSTPIP1) (Liu et al., 2015). The central SH2 domain of FER mediates interactions with substrates that are subsequently phosphorylated by the carboxy-terminal kinase domain (Greer, 2002). Although several FER targets have been identified, including Src (Oneyama et al., 2016), Cortactin, p120-catenin, and β-catenin (Kim and Wong, 1995, 1998), it remained unclear if these targets were subject to direct phosphorylation by FER.

FER controls cell migration and invasion, possibly through modulation of cortactin function and integrin-dependent control of actomyosin contraction (Arregui et al., 2000; Ivanova et al., 2013). Although it is clear that downregulation or inactivation of FER leads to a G0/G1 cell-cycle arrest, anchorage-independent survival, and a strong inhibition of migration (Ivanova et al., 2013; Sangrar et al., 2007), the exact mechanisms continued to be largely unidentified. In breast cancer, FER controls migration and metastasis by regulating α6 and β1 integrin-dependent adhesion (Ivanova et al., 2013). Because FER depletion resulted in the accumulation of α6 and β1integrins in early endosomes (EEs) and plasma membrane, it suggests that endosomal recycling and/or intracellular trafficking is central to FER-dependent proliferative and migratory cues.

Plasma membrane homeostasis is tightly regulated by continued endocytosis and endosomal sorting, resulting in an intricate balance of protein recycling and degradation (Cullen and Steinberg, 2018). Recycling of membrane receptors occurs through multiple routes and is tightly regulated by Ras-like in rat brain (Rab) proteins, small GTPases that associate and coordinate membrane trafficking. Fast recycling promotes rapid delivery of Rab4-positive endosomes from EEs (EE antigen 1 [EEA1]/Rab5) to the plasma membrane. Slow recycling relocates molecules to Rab11-positive recycling endosomes prior to re-localizing to the cell surface (Sönnichsen et al., 2000). It is, however, unclear if and how FER controls its kinase substrates to regulate endosomal sorting/recycling, processes essential for the invasion and dissemination of cancer cells.

Here, we have used clinical data to identify FER as a candidate predictor of taxane-containing adjuvant-chemotherapy benefits in high-risk breast cancer. A combination of phospho-proteomics, chemical genetics, and functional cell biology was applied to study the mechanisms underlying FER-dependent breast cancer invasion. Our work demonstrates that FER controls endosomal recycling and may represent a predictive clinical biomarker of taxane efficacy in high-risk breast cancer, including TNBC.

RESULTS

The phospho-proteome downstream of FER

Previously, we have shown that the tyrosine kinase FER propels migration and metastasis of TNBC cells in mice and established FER as a promising target for inhibition of metastatic breast cancer (Ivanova et al., 2013). To identify options for therapeutic intervention of FER-driven processes, we analyzed the phospho-proteome downstream of FER. For this we used doxycycline (DOX)-inducible FER knockdown MDA-MB-231 cells (MM231-FERiKD) (Figure 1A; Ivanova et al., 2013) in combination with a stable isotope labeling by amino acids in cell culture (SILAC) approach. Mass spectrometry (MS) analysis identified a total of 202 unique phospho-sites on 141 proteins that were differentially regulated in FER-depleted cells (Table S2A). We detected the majority of phosphorylation events on serine and threonine residues, with a small fraction (<1%) occurring on tyrosines (Table S2A). Major changes upon FER depletion were observed in phosphorylated tyrosine (pTyr) residues (Figures 1B and 1B′), of which 8.3% were upregulated and 91.7% were downregulated, followed by phosphorylated serine (pSer) residues (up, 32.6% and down, 57.4%) and phosphorylated threonine (pThr) residues (up, 40% and down, 60%) (Figure 1B'). Because epidermal growth factor receptor (EGFR) has been described as a downstream target of FER (Guo and Stark, 2011), phosphorylation of EGFR on Y1173 was used to confirm the SILAC results. Indeed, FER depletion resulted in an 8-fold reduction in phosphorylation (Figure 1C). Interestingly, Gene Ontology (GO) terms and reactome pathway enrichment analyses showed a significant enrichment in "Cell Cycle, Mitotic" (false discovery rate [FDR] = 3.9×10^{-4}) and "Membrane Trafficking" (FDR = 5.8×10^{-4}) pathways (Figures 1D and 1E; Table S2B). Examples of affected proteins in these pathways are KIF2A and KIF11, known mediators of microtubule (MT) dynamics (Homma et al., 2003; Rapley et al., 2008).

Together, these results show that FER phosphorylates several proteins involved in the regulation of MT-dependent processes: membrane trafficking and proliferation.

High FER expression predicts increased sensitivity to MT-stabilizer drugs

The possible reliance of MT-dependent processes like protein trafficking on FER kinase instigated our hypothesis that high FER levels in basal breast cancer cells could render cancer cells more sensitive to MT-stabilizing drugs, e.g., taxanes.

To test this, we compared docetaxel and paclitaxel efficacy on proliferation inhibition using basal MDA-MB-468 (MM468), SUM149PT, and MM231 cells expressing different FER levels (Figures 2A and S1A). Strikingly, high-FER MM231 cells displayed a 9-fold higher sensitivity to docetaxel (Figure 2B; half maximal inhibitory concentration [IC50] = 0.63 versus 5.7 nM) and paclitaxel when compared with MM468 cells (Figure S1B; IC50 = 0.93 versus 4.67 nM). SUM149PT cells exhibit intermediate levels of FER protein and response to docetaxel (IC50 = 2.5 nM). To establish causality, MM231-FERiKD cells were used to analyze the effect of FER depletion on docetaxel and paclitaxel sensitivity. Indeed, FER depletion caused a significant increase in docetaxel (Figure 2C) and paclitaxel resistance (Figure S1C).

To test clinical relevance, we explored if high FER expression in breast cancer is predictive for patient outcome after taxane treatment. We analyzed gene expression data from the MATADOR study (van Rossum et al., 2018), a randomized phase III clinical trial in which 664 patients were treated with either adjuvant dose-dense doxorubicin + cyclophosphamide (ddAC) or AC combined with docetaxel (TAC). The median follow up was 7 years. We found that in patients with low FER levels, no difference in outcome was observed between adjuvant TAC and ddAC (adjusted hazard ratio [adjHR] = 1.08; 95% confidence interval [CI]: 0.64–1.84, p = 0.76) (Figure 2D). In contrast, high FER levels correlated with an increased probability of recurrence-free survival (RFS) following taxane-containing treatment, compared with ddAC-only treatment (adjHR = 0.48; 95% CI: 0.24–0.96; p = 0.039) (Figure 2E). The test for interaction was, however, not statistically significant (p = 0.06). To further analyze the predictive value of FER expression, we grouped patients according to their immunohistochemical profile (TNBC and $ER^{POS}HER2^{NEG}$ ["luminal"] subtypes) (Figures 2D, 2E, S1D, and S1E). Despite the

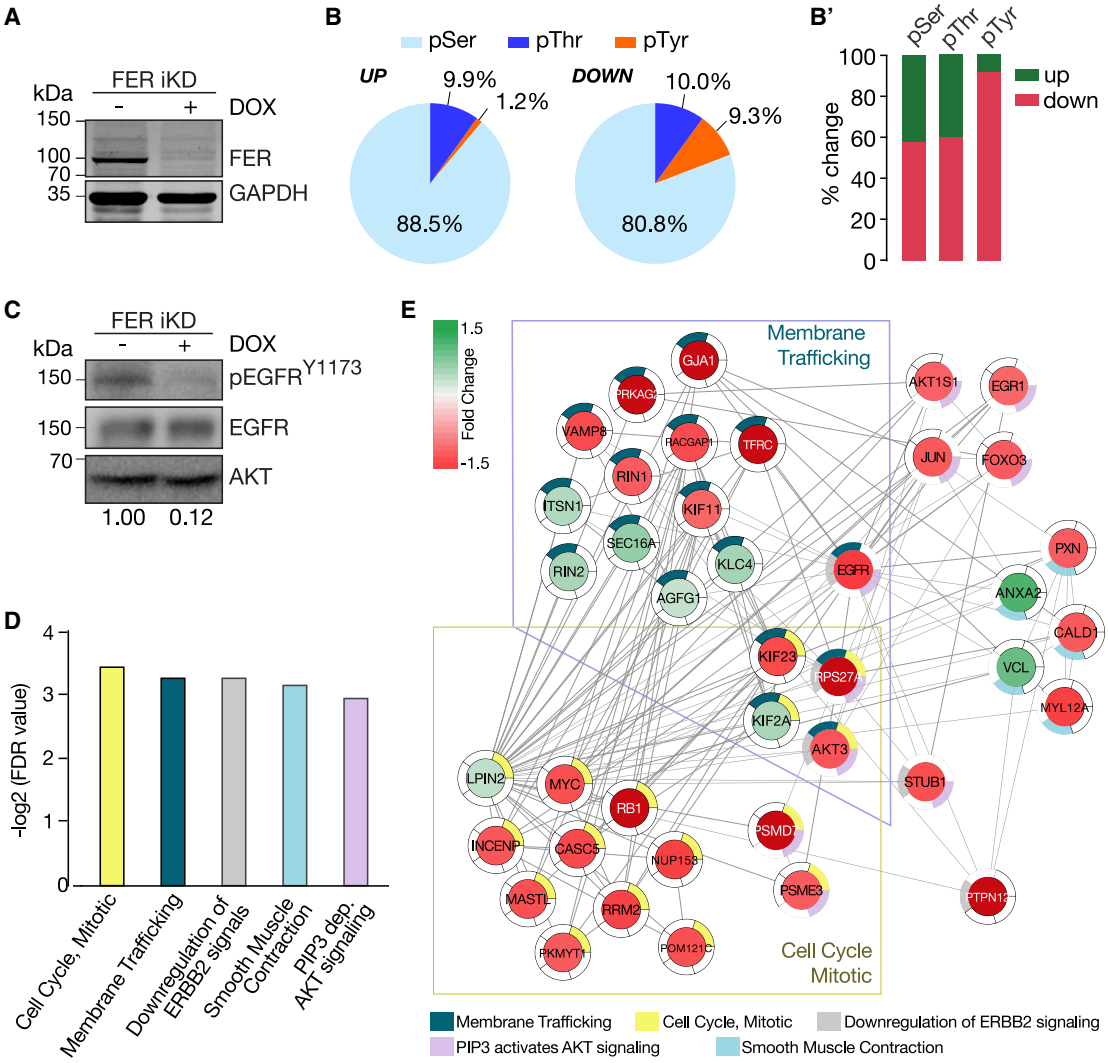

Figure 1. FER depletion attenuates cell-cycle progression and vesicle trafficking pathways

(A) FER knockdown in MM231. FER-iKD cells were treated with DOX, blotted, and probed with anti-FER antibody. GAPDH was used as loading control.

(B and B′) The effect of FER depletion on post-translational phosphorylation using SILAC.

(B) Shown are the ratios of serine (light blue), threonine (dark blue), or tyrosine (orange) residues in all phospho-sites enriched (left) or decreased (right) after FER-iKD in MM231.

(B′) Shown are the ratios of serine, threonine, or tyrosine residues phospho-sites enriched (green) or decreased (red) after FER-iKD in MM231. Ratio of serine, threonine, or tyrosine residues shown is averaged from 3 phospho-proteomes.

(C) Phosphorylation of EGFR was used as a validation for the SILAC experiments in (B)–(D). Western blot showing the extent of EGFR downregulation of pTyr on residue Y1173 using a phospho-specific antibody. EGFR and AKT expression were used as loading controls. Numbers below the panel indicate the $pEGFR^{Y1173}$ signal in control and DOX-treated MM231 FER-iKD cells.

(D) From (B), the top 5 GO biological processes controlled by FER were derived. The x axis represents the log to base 2 of the false discovery rate (FDR) levels.

(E) Subnetworks of phosphorylated proteins involved in the top 5 reactome pathways, as identified by SILAC. Node colors represent fold-change regulation at the phosphorylation level (upregulation [green] or downregulation [red]), while the node border color represents the biological process involved.

See also Table S2.

relatively low number of TNBC patients (n = 87), high FER levels were correlated with a significant lower probability of recurrence when treated with TAC versus ddAC in this subgroup (adjHR = 0.079; 95% CI: 0.007–0.92; p = 0.043) (Figure 2E). For patients with TNBC tumors expressing low FER levels, there was no significant RFS difference when comparing the two treatment arms (Figure 2D). Together, these data support that high FER levels could be a predictor for sensitivity to taxane drugs in high-risk breast cancers, including TNBC.

FER phosphorylates regulators of proliferation and protein recycling

Our previous work and current observations prompted us to further explore FER-driven mechanisms underlying TNBC cells

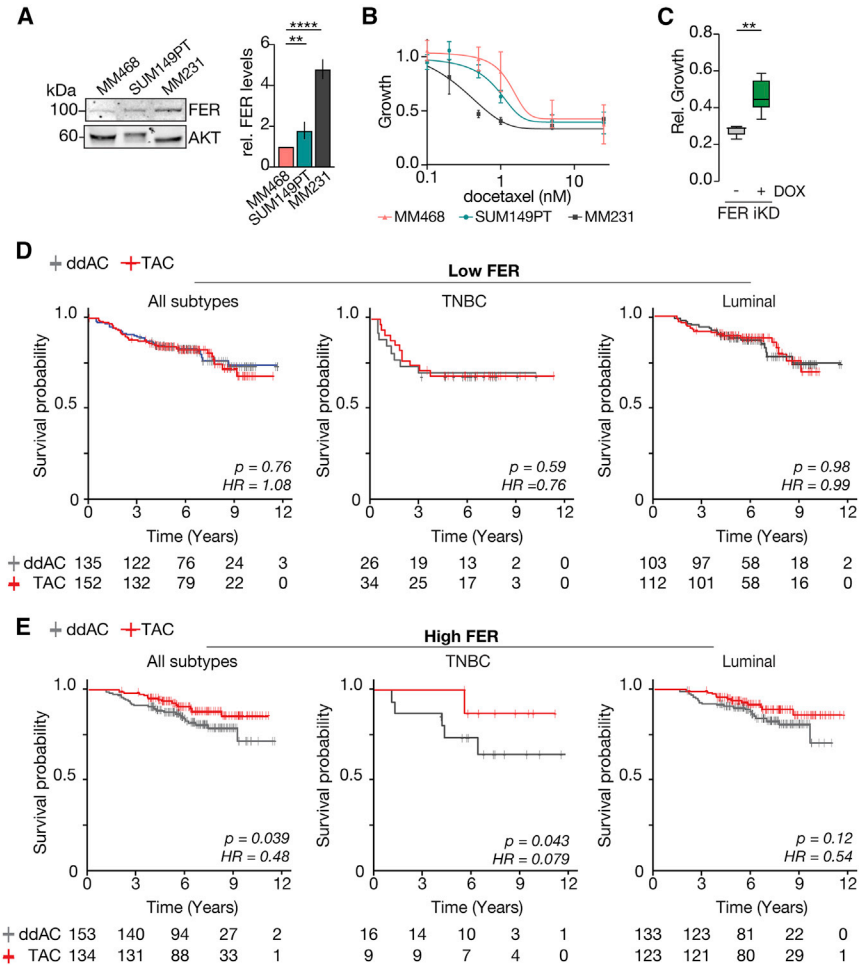

Figure 2. High FER expression is a candidate predictive biomarker of taxane-based treatment in high-risk HER2-negative breast cancer

FER induces docetaxel sensitivity.

(A) FER protein expression in the basal breast cancer cells MM468, SUM149PT, and MM231. Quantifications of western blot analyses are shown in the right panel. AKT was used as loading control.

(B) Dose-response surviving fraction curves of MM468 cells (red), SUM149PT (green), and MM231 (gray) treated with increasing doses of docetaxel.

(C) FER controls taxane responses in basal breast cancer cells. MM231 FER iKD cells were treated with 1 nM docetaxel in the context of DOX administration. Error bars indicate SD; **$p < 0.01$.

(D and E) Exploratory analysis of FER mRNA expression as predictive biomarker for taxane-containing adjuvant chemotherapy benefit. Recurrence-free survival probability of patients with breast cancer (BC) expressing low (D) or high (E) FER mRNA levels from all patients (left panels), TNBC (center panels), or the ER^+HER2^- ("luminal") subtype (right panels). Information includes number of patients in each group at certain time intervals. Patients were treated with either ddAC (gray) or TAC (red) adjuvant chemotherapy. HR, adjusted hazard ratio.

See also Figure S1.

response to taxanes. Hence, we performed direct FER-substrate analysis using chemical genetics (Bishop et al., 2000). For this, we identified a conserved methionine at position 637 (M637) as a potential gatekeeper residue of the FER ATP-binding pocket (Figures 3A and 3B). Considering the substantial homology and structural similarity between FES and FER (Matsuura, 2019), we inferred the FER structure based on an FES structure (Filippakopoulos et al., 2008) (Figure 3C). Because full-length FER cannot be produced in prokaryotes (Greer, 2002), we generated truncated forms of the analog-sensitive M637A (FER-AS) allele; wild-type (WT) and kinase-deficient (D742R) FER. The SH2- and kinase-domain-containing truncates were expressed and purified as GST-fusion proteins for *in vitro* assays to test kinase activity using ATPγS (Figure 3D) and "bulky" ATPγS analogs (Hertz et al., 2010) (Figure 3E). FER autophosphorylation was used as positive control, and recombinant cortactin was used as a potential control substrate based on published observations (Sangrar et al., 2007) (Figure 3D). Importantly, FER-AS was susceptible to the cell-permeable inhibitor NM-PP1 (Figure 3F). NM-PP1 treatment blocked FER autophosphorylation and phosphorylation of cortactin (Figure 3F), thus identifying cortactin as a direct FER kinase substrate *in vitro*. As predicted, FER-AS could utilize a variety of bulkyATPγS analogs, of which N^6-furfuryl-ATPγS and N^6-benzyl-ATPγS were most efficiently thio-phosphorylated (Figure 3G).

Using functional FER-AS and N^6-benzyl-ATPγS, we performed substrate labeling in MM231 whole-cell lysates (Figure 3H). Analysis of the purified thio-phosphopeptides using MS revealed the identity and location of multiple pTyr sites on 16 tagged peptides. Among these, we identified 6 substrates that are involved in cytoskeletal rearrangement, transcriptional regulation, cell proliferation, and vesicular trafficking (Table S1). The identified FER autophosphorylation sites were considered internal positive controls. Our data also confirmed phosphorylation of the FER activation loop at Y714 (Oneyama et al., 2016), the SH2 domain (Y492, Y497), and the kinase domain (Y615) (Hikri et al., 2009) (Table S1). Interestingly, three autophosphorylation sites were identified in domains crucial for FER kinase activity. One site corresponded to Y532 in the SH2 domain while the other two sites were mapped to Y578 and Y799 in the FER catalytic domain (Table S1). We also identified Y357 phosphorylation in αTubulin (TUBA1B), a substrate previously implicated as a direct FER target (Shapovalova et al., 2007). Among the 6 direct FER targets identified, two were MAPK1 and DCTN2 (also known as Dynamitin/p50), proteins implicated in cellular proliferation and membrane trafficking, respectively. As such, we have successfully developed an analog-sensitive model system for FER kinase and identified direct FER targets using a chemical genetics approach.

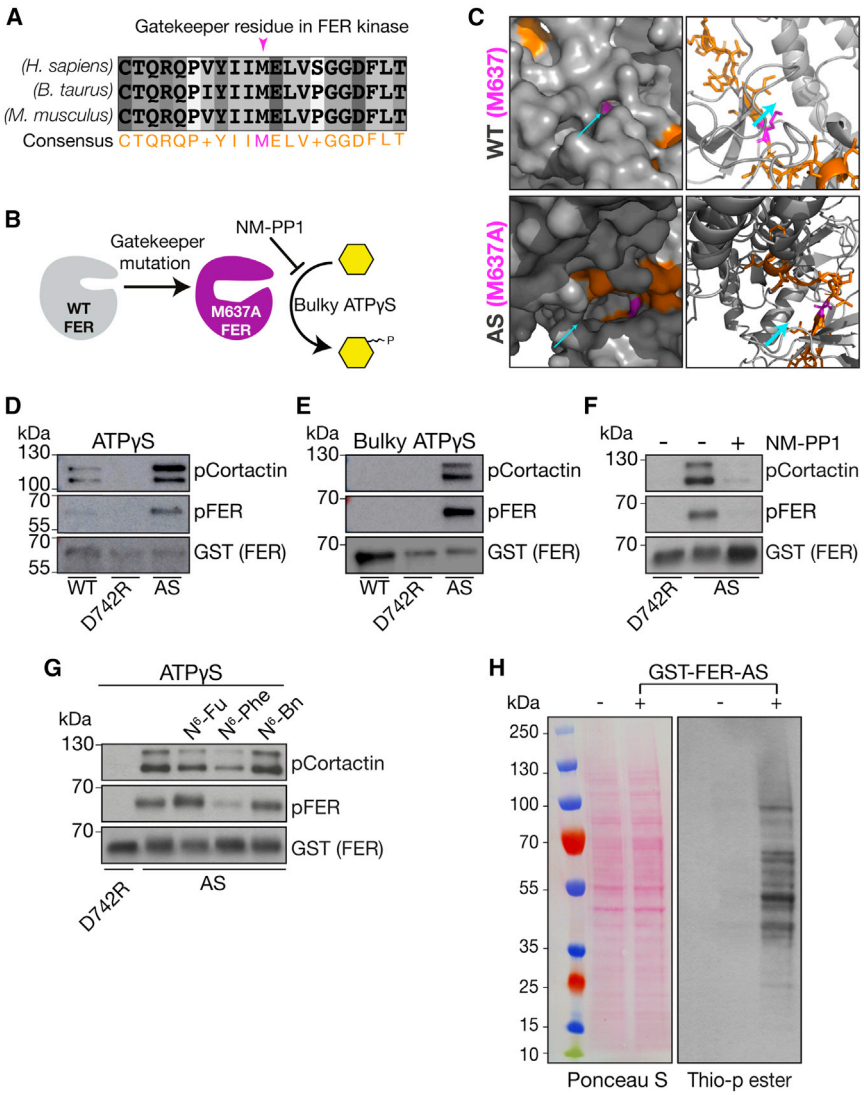

Figure 3. Analog-sensitive FER (FER-AS) phosphorylates trafficking and cytoskeleton regulators

(A) Identification of the gatekeeper residue. Sequence alignment of the kinase domain hinge region and conservation of the gatekeeper residue in FER. Consensus sequence (orange) and the gatekeeper methionine residue at position 637 (M637) (magenta) are shown.

(B) Schematic view on the chemical genetics approach.

(C) Surface representation of FER-wild type (WT) and FER-AS inferred from the FES structure. Zoom-in surface (left panels) and ribbon representation (right panels) of the ATP pocket show the details of the gatekeeper pocket. The gatekeeper residue (magenta), peptide backbone (gray), and consensus sequences (orange) are shown.

(D and E) FER-AS phosphorylates cortactin *in vitro*. Kinase assays with recombinant GST-tagged WT, kinase dead (D742R), or FER-AS in the presence of ATPγS (D) or N^6-benzyl-ATPγS (E).

(F) Inhibition of tyrosine kinase activity in FER-AS. Kinase assays with recombinant FER D742R and FER-AS in the presence of ATPγS and NM-PP1 (15 μM).

(G) Incorporation of "bulky" ATP by FER-AS. Kinase assays with FER-D742R or FER-AS in the presence of ATPγS, N^6-furfuryl(Fu)-ATPγS, N^6-phenylethyl(Phe)-ATPγS, or N^6-benzyl(Bn)-ATPγS. GST-FER served as loading control in (D)–(G).

(H) Kinase assay using FER-AS in the presence of N^6-Fu-ATPγS on protein extracts from MM231. Equal loading was confirmed by Ponceau S staining. Direct thiophosphorylated (p) substrates and auto-(thio)phosphorylated FER were detected with anti-thiophosphate ester.

See also Table S1.

Control over tumor progression features by FER is tyrosine kinase dependent

To determine whether the oncogenic FER functions rely on its tyrosine kinase activity, we reconstituted FER-iKD cells with a DOX-inducible, full-length, and RNAi-resistant version of FER-AS. Upon DOX, we could reach near-endogenous levels in FER-AS-reconstituted MM231 cells (FER^{RECON}; Figures 4A, S2A, and S2B). In control cells, FER was mostly concentrated at the perinuclear area and within protrusive structures (Figure 4B). Interestingly, NM-PP1 treatment resulted in a homogeneous distribution of FER throughout the cytoplasm (Figure 4B).

During cancer progression, cells detach, invade surrounding tissues, and disseminate to distant organs. These metastatic steps are interrelated and dependent on cell adhesion. To probe whether cancer cell adhesion is dependent on the tyrosine kinase activity of FER, we employed FER^{RECON} cells. While FER depletion led to overt cell spreading followed by formation of abundant focal adhesion (FA) sites, using phospho-Paxillin (pPax) localization as a readout (Figures 4C and S2C), FER^{RECON} rescued FER loss, resulting in motile cells characterized by sporadic FA formation and absence of F-actin stress fibers (Figures 4C, 4D, and S2C). Kinase inhibition using NM-PP1 largely abolished the migratory phenotype (Figures 4C and 4D) and associated with an increase in FA formation (Figure 4E).

Next, we analyzed the contribution of the tyrosine kinase activity of FER to cell-cycle progression. FER depletion led to a 50% reduction of dividing (S-phase) cells (Figures 4F and 4G). Upon DOX treatment, FER^{RECON} cells exhibited a rescue of their proliferative potential (Figures 4F and 4G). Treatment of FER^{RECON} cells with DOX and/or NM-PP1 resulted in an approximate 30% reduction of dividing cells (Figures 4F, 4G, S2D, and S2E), coinciding with a decrease of FER^{RECON} cell numbers (Figure 4H). Moreover, we observed 3D cell invasion was fully inhibited in the presence of DOX and NM-PP1 (Figure 4I) whereas cells treated with NM-PP1 showed 3D invasion resembling the control condition (Figure S2F). Also, NM-PP1 did not influence growth of FER^{RECON} cells in the absence of DOX (Figures S2D–S2H). Interestingly, FER-AS kinase inhibition

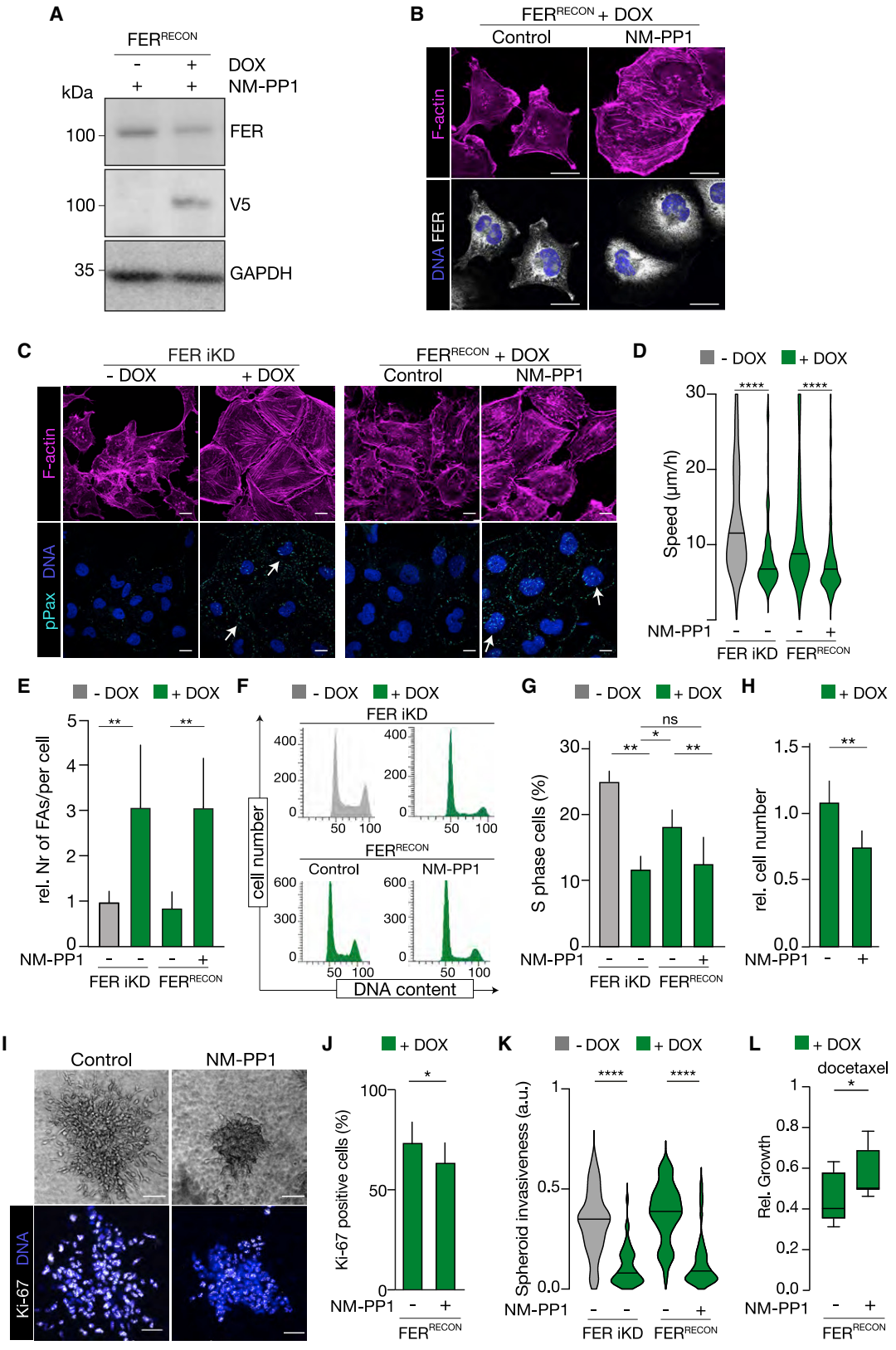

(legend on next page)

resulted in a reduction in spheroid size, which could be attributed to impaired cell proliferation upon treatment with both DOX and NM-PP1 (Figures 4I and 4J). In the absence of DOX treatment, NM-PP1 did not influence growth of FER^{RECON} cells (Figures S2G and 2H). Moreover, both FER loss and FER-AS kinase inhibition results in a reduction in the invasive potential (Figure 4K). Importantly, specific inhibition of FER kinase activity using NM-PP1 leads to a decrease in docetaxel-induced cytotoxicity (Figure 4L), indicating that FER-dependent oncogenic triggers and responses to taxanes are largely dependent on its tyrosine kinase activity. In short, high FER expression and activity underpin taxane responses in TNBC cells.

Since Y187 on MAPK1 was identified as a putative FER phosphorylation site (Table S1), we assessed MAPK1 phosphorylation downstream of FER kinase activity. Validation kinase assays were performed employing NM-PP1, resulting in specific inhibition of FER-AS-dependent pTyr of MAPK (Figure S3A). Using whole-cell lysates and a combination of coimmunoprecipitation (coIP) with MAPK1/3-specific and pan tyrosine phosphorylation antibodies, we found that FER loss or inactivation significantly reduced MAPK1 pTyr (Figures S3B and S3C, respectively). MAPK1 was indeed phosphorylated on the Y187 residue (Figure S3; co-localization of the red pY20 and green pMAPK1 signal). The obtained NM-PP1-induced reduction of MAPK1 Y187 phosphorylation, when compared with the contribution of MAPK1 phosphorylation by the MEK1 inhibitor (MEKi) selumetinib, suggested that approximately 20%–30% of the total MAPK1 activation on Y187 in MM231 cells is through direct phosphorylation by FER kinase (Figure S3G). Together with the downregulation in EGFR phosphorylation observed by SILAC upon FER KD (Figures 1C and 1E), our data suggest a dual regulation of FER on MAPK signaling: first, indirectly through the downregulation of EGFR activation and second, directly through the phosphorylation of MAPK1.

Another FER substrate associated with proliferation and membrane trafficking was αTubulin (Table S1). Using *in vitro* kinase assays, we could confirm αTubulin as a genuine FER target (Figure S4A). We therefore also tested whether FER depletion impacted MT stability, but we observed no changes in the abundance of either CAMSAP2-stabilized MT minus ends (Figure S4B) or de-tyrosinated MTs (Figure S4C). We therefore conclude that FER-induced sensitivity to taxanes is not caused by direct control of FER on MT stability.

FER depletion affects integrin recycling

Because our biochemical data indicated a role for FER-dependent membrane/protein trafficking, we studied the effect of FER loss on endosomal and lysosomal processes using endocytic uptake and endosomal sorting of BSA (lysosome-directed cargo). Co-localization analysis with the EE marker EEA1 and the lysosomal membrane protein LAMP1 (Figures 5A and S5A, respectively) did not show BSA accumulation in EEs or lysosomal alterations in DOX-treated cells, indicating that endocytic uptake and transport of BSA to lysosomes is independent of FER. We also visualized acidified late endosomes and lysosomes by cell-permeable SiR lysosomes in live cells and found no significant differences in lysosomal vesicle trafficking upon FER loss (Figure 5B). Furthermore, endogenous LAMP1 labeling showed no effects on steady-state spatial distribution of lysosomes upon FER depletion, whereby lysosomes retained their predominant localization in the perinuclear area upon DOX (Figure 5C). Loss of FER did not affect co-localization between LAMP1 and α6 integrin (Figure 5D), indicating normal transport and degradation of α6 integrin to lysosomes. Together, these results show that FER neither controls transport of endocytosed cargo to lysosomes nor causes aberrations in lysosome acidification, transport, or lysosomal degradation.

Next, we assessed the impact of FER depletion on endosomal recycling. Cells were incubated with the recycling marker transferrin (TF) and co-stained with EEA1 (Cullen and Steinberg, 2018), which showed an accumulation of TF in EEA1-positive EEs upon FER depletion (Figures 5E and 5F). Given the previous observation that α6 and β1 integrin localizations are controlled by FER (Ivanova et al., 2013), we analyzed co-localization of these integrins with EEA1 and observed a significant accumulation in EEs in the absence of FER (Figures 5E–5G, S5B, and S5C). Importantly, FER kinase inhibition in FER^{RECON} cells using NM-PP1 also induced an increased accumulation of TF in EEs when compared with control FER^{RECON} cells (Figures 5H, 5I, S5D, and S5E). Hence, our data show that cargo recycling from EEs depends on the kinase activity of FER.

Figure 4. A reconstitution model to study how FER kinase activity controls BC progression

(A) MM231 FER iKD cells were stably reconstituted to endogenous levels with an FER-AS mutant (FER^{RECON}). Expression levels of reconstituted and WT FER were assessed using FER and V5-tag antibodies (V5). GAPDH was used as loading control.

(B) FER^{RECON} is functional. FER^{RECON} cells treated with DOX and NM-PP1 and probed for F-actin (magenta), FER (white), and DNA (DAPI, blue) using immunofluorescence (IF). Scale bars, 15 μm.

(C–E) FER kinase activity is essential for cell motility. (C) IF confocal images showing the effect of FER kinase inhibition on cell motility. The velocity of individual cells was quantified upon FER depletion or after inhibition of the tyrosine kinase activity with NM-PP1 using live-imaging (D). Phosphorylation of Paxillin (p-Pax, cyan) was used to illustrate the sessile adhesive phenotype and the presence of FAs (arrows), which were quantified in (E). Scale bars, 15 μm.

(F and G) FER^{RECON} cells were used for cell-cycle profiling, and the percentage of cells in S phase was determined.

(H) FER^{RECON} cells were treated as indicated and the effect of FER kinase activity of cell proliferation was determined using colony formation assays.

(I–K) FER kinase is essential for the invasive growth of BC cells in 3D. FER^{RECON} cells were plated as tumor spheroids in collagen-I gels, imaged after administration of DOX and/or NM-PP1 (phase contrast; I), and stained for Ki-67 (J). Quantifications of tumor spheroid invasiveness are shown in (K). Scale bars, 50 μm. Quantifications are from at least three biological replicates.

(L) Taxane responses in basal BC cells are FER kinase dependent. FER^{RECON} cells were treated with 0.5 nM docetaxel in the context of DOX and NMPP1 administration.

Error bars indicate SD; ns indicates non-significant; *$p < 0.05$, **$p < 0.01$, and ****$p < 0.0001$. Statistical significance was calculated using one-way ANOVA. See also Figures S2, S3, and S4.

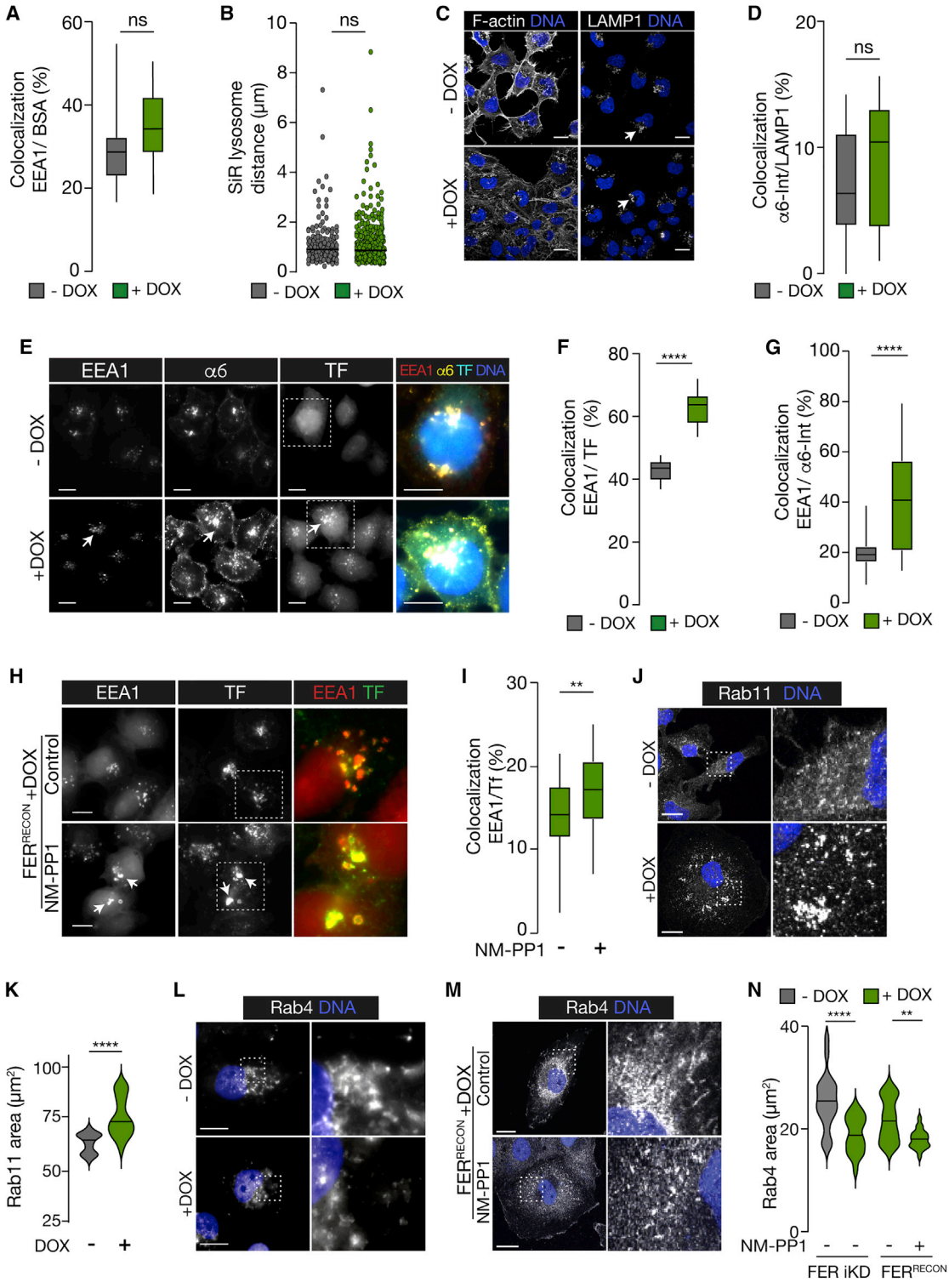

Figure 5. FER controls endosomal recycling/trafficking

(A–D) FER does not control endocytosis or lysosomal function. Co-localization studies of MM231 FER iKD treated with or without DOX were incubated with BSA and stained with anti-EEA1. Quantification of BSA and EEA1 co-localization is shown in (A). (B) Trajectory lengths were measured of SiR-lysosome-positive vesicles in MM231 FER iKD treated with or without DOX. MM231 FER iKD cells were treated with DOX and stained for F-actin (left panel) or LAMP1 (right panel) (C). White arrows highlight the similarity of the LAMP1-positive vesicles in the absence or presence of DOX. Quantification of integrin α6 and anti-LAMP1 colocalization is shown in (D).

(legend continued on next page)

We then analyzed the formation of recycling vesicles by immuno-localization of endogenous Rab11 and Rab4 (McCaffrey et al., 2001). Rab4 marks early-stage recycling tubules that form at the early-endosomal vacuole and travel either directly to the plasma membrane or to specialized, Rab11-positive recycling endosomes (van der Sluijs et al., 1992; Ullrich et al., 1996). Interestingly, FER-depleted cells showed an increase in Rab11-positive vesicles (Figures 5J and 5K) and a collapse of Rab4-positive membranes compared with control cells (Figures 5L and 5N). This was dependent on the kinase activity of FER, as inhibition using NM-PP1 also led to abrogation of Rab4-expressing structures (Figures 5M and 5N).

Together, the findings that recycling cargo accumulates in EEA1-positive endosomes and that the collapse of the Rab4-recycling tubules upon FER depletion indicate that FER is involved in kinase-dependent protein sorting and/or tubule formation at early-sorting endosomes.

DCTN2 is a candidate intermediate of FER kinase activity and endosomal recycling

Because FER controls endosomal recycling/sorting and endosomal recycling relies on MT-dependent transport (Caviston and Holzbaur, 2006), we focused on the FER substrate DCTN2 (Table S1). DCTN2 is an integral part of the dynactin complex (Valetti et al., 1999), which is essential for MT minus-end-directed transport of membrane organelles (Liu, 2017). First, kinase assays were performed using recombinant GST::DCTN2 fusion proteins, which confirmed that FER-AS phosphorylates DCTN2 *in vitro* (Figure 6A). To functionally assess a contribution of DCTN2 to tumor progression, we performed loss-of-function experiments using two lentiviral DOX-inducible hairpins (Figure 6B). Upon DOX addition, we observed sessile phenotypes that overlapped with those observed in FER-depleted cells: extensive cell spreading, stress fiber formation, larger, more abundant FAs in interphase cells, and decreased migration speed (Figures 6C–6F). Next, we reconstituted DCTN2-depleted cells with GFP-tagged versions of WT DCTN2 (GFP-DCTN2^{WT}) or DCTN2 mutant Y6A (GFP-DCTN2^{Y6A}) (Figure 6G) because Tyr6 of DCTN2 was identified as a potential FER kinase phosphorylation site (Table S1). DCTN2-Y6 resides in the interaction surface with ARP1 in the dynactin complex; its replacement by an alanine might thus affect dynactin-dynein complex formation or function (Figures S6A–S6D). To investigate this, we co-immunoprecipitated GFP-tagged DCTN2 proteins (Figure S6E) and blotted for dynein intermediate chain and ARP1 (Figure 6H), a dynein complex component that mediates the binding of dynein to dynactin (Vaughan et al., 2001). Indeed, MM231 cells reconstituted with GFP-DCTN2^{Y6A} showed an approximate 50% reduction in the ability to interact with ARP1 and dynein when compared with cells rescued with GFP-DCTN2^{WT} (Figure 6I).

We next functionally tested DCTN2^{WT} or DCTN2^{Y6A} reconstituted cells in the context of 2D adhesion. While DCTN2^{WT} rescued the phenotype induced by DCTN2 iKD (Figures 7A and 7B), DCTN2^{Y6A} failed to functionally reconstitute DCTN2, leading to overt cell spreading, increased FA formation (Figures 7A and 7B), and decreased cell migration speed (Figure 7C). These observations suggested that the DCTN2-Y6 residue is important for the motility of MM231 cells. Moreover, reconstitution with the DCTN2-Y6A mutant failed to fully restore cellular invasion upon DCTN2 depletion (Figures 7D' and 7D″), indicating that DCTN2^{Y6} is essential for the motility, invasion, and growth of MM231 cells.

To study if endosomal recycling tubule formation is dependent on DCTN2 and its Y6 residue, we visualized recycling tubules on sorting endosomes using Rab4 in conjunction with EEA1 and observed that DCNT2 depletion caused an abrogation of endosomal tubular structures (Figures 7E and 7G) and an accumulation of EEA1 in the perinuclear area (Figure 7E), phenocopying loss of FER function (Figures 5L–5N). Also, while reconstitution of GFP-DCTN2^{WT} rescued Rab4-positive structures, GFP-DCTN2^{Y6A} reconstituted cells showed severely impaired Rab4 recycling tubule formation (Figures 7F and 7G). In contrast to DCTN2^{WT}, mutation of DCTN2^{Y6} did not rescue proper β1 integrin localization, leading to an accumulation of β1 integrin in EEA1 vesicles (Figure 7H).

We next analyzed if the Y6A mutation confers an effect on taxane sensitivity using the DCTN2^{WT} and DCTN2^{Y6A} reconstituted breast cancer cells. Cells were treated with two different docetaxel concentrations, and cellular proliferation was followed over time. Interestingly, we find that reconstitution with the DCTN2^{Y6A} mutant does not significantly impact the growth reduction caused by docetaxel (Figure S6F). In sum, these results suggest that DCTN2 specifically regulates endosomal recycling circuitry to promote FER-dependent migration and invasion of TNBC cells.

DISCUSSION

Since MTs are intricately involved in and necessary for vesicular trafficking, and early endosomal function is controlled by FER kinase, we assessed the efficacy of MT-stabilizing drugs in the context of FER. Our preclinical findings were corroborated in the clinical MATADOR trial, suggesting that high FER mRNA

(E–G) FER controls endosomal recycling. MM231 iKD cells were treated with DOX and incubated with fluorophore-conjugated transferrin (TF). EEA1 (red), TF (cyan), and α6 integrin expression (α6; yellow) were visualized in (E), and co-localization was quantified (F and G). Inset images correspond to a 240% magnification.

(H and I) FER controls endosomal recycling through its kinase activity. FER^{RECON} cells were treated with DOX and NM-PP1 and incubated with TF-647 (green). Cells were stained for EEA1 (red; H), and co-localization with TF was quantified in (I). Inset images correspond to a 240% magnification.

(J and K) FER differentially controls the formation of Rab11-positive recycling tubules. MM231 FER iKD cells were treated with DOX and stained for Rab11 (J). Quantification of area of Rab11-positive vesicles is shown in (K).

(L–N) FER activity controls formation of Rab4 positive tubules. FER iKD (L) or FER^{RECON} (M) cells were treated with DOX and NM-PP1 and were stained for Rab4 (white). Inset images correspond to a 175% magnification. Scale bars = 15 μm. Quantifications of the Rab4-positive vesicle areas are shown in (N).

Error bars indicate SD; ns indicates non-significant; $^{**}p < 0.01$ and $^{****}p < 0.0001$.

See also Figure S5.

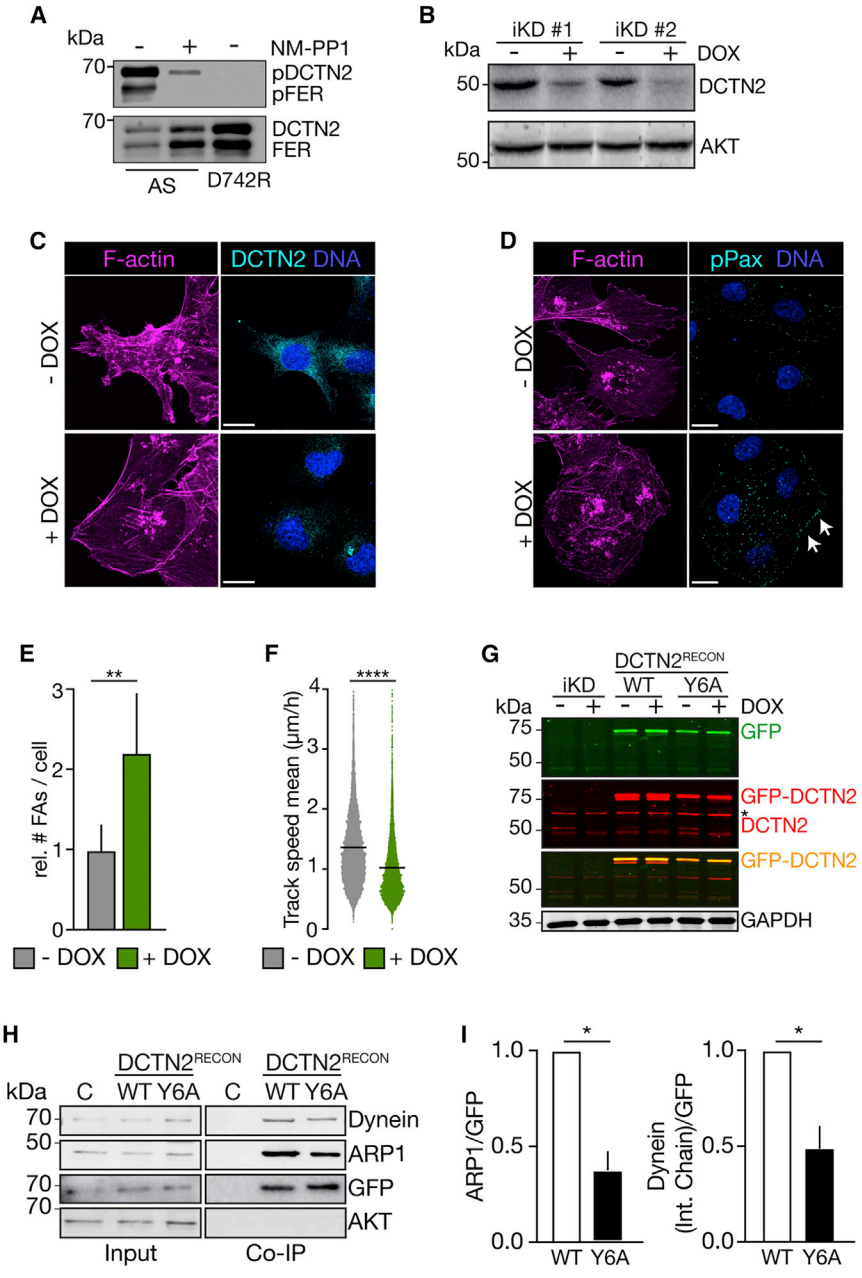

Figure 6. DCTN2 is a candidate FER tyrosine kinase substrate

(A) DCNT2 is a direct FER substrate. Shown are kinase assays using FER-D742R and FER-AS in the presence of ATPγS, using recombinant GST-DCTN2 as substrate. GST-FER served as loading control.

(B–F) DCNT2 is essential for BC cells motility. DCTN2 was knocked down in MM231 cells using two independent DOX-inducible shRNA sequences (B), and cells were stained for DCTN2 (cyan) (C) or p-Paxillin (D). Scale bars, 50 µm. The effect on FA formation was quantified in (E). (F) Live fluorescence imaging of MM231 DCTN1iKD cells transfected with pGK-GFP ± DOX grown in 2D. Migration speed was quantified.

(G–I) The N-terminal Y6 residue of DCTN2 controls dynactin complex formation. DCTN2-iKD cells were reconstituted with either DCTN2 WT ($DCTN2^{RECON}$-WT) or the alanine substitute $DCTN2^{Y6A}$ ($DCTN2^{RECON}$-Y6A) (G), whereby GAPDH was used as loading control (asterisk indicates unspecific band). Dynactin complex formation was assessed using coIP and western blotting (H and I). Parental MM231 cell lysates were used as non-specific immunoprecipitation controls. Blots were blotted with anti-dynein (Intermediate Chain), anti-ARP1, anti-GFP, and anti-AKT as loading controls for input samples. Quantification of levels of dynein and ARP1 bound to GFP-DCTN2-WT and GFP-DCTN2-Y6A was performed. Error bars indicate SD; *p < 0.05. Statistical significance was calculated using Student's t test.

See also Figure S6.

levels predict the benefit of adjuvant taxane-containing chemotherapy in high-risk breast cancer. Provided these findings can be confirmed in an independent cohort, this provides substantial ramifications for the clinical management of aggressive breast cancer types using chemotherapy. As FER does not affect MT stability, our data suggest that breast cancers expressing elevated FER levels strongly rely on MT-dependent cell processes. Based on our work, we propose that next to the obvious effects on mitosis, endosomal recycling represents an additional and essential process during tumor invasion that is controlled by FER kinase activity.

Endosomal trafficking is a crucial process that regulates the activation of major signaling pathways driving proliferation, migration, and invasion. It has been suggested that cancer cells upregulate recycling pathways to re-use growth factor receptors instead of targeting them to lysosomes for degradation, a shift that results in prolonged signaling and increased proliferation (Eden et al., 2010; Lonic et al., 2021; Rafn and Kallunki, 2012).

Formation of recycling tubules starts by the induction of membrane curvature on sorting endosomes. Local membrane deformation subsequently recruits F-BAR-containing proteins that regulate nascent tubule elongation (Delevoye et al., 2016). Although FER contains an F-BAR domain, it is not a strong inducer of membrane curvature but instead mainly acts as a curvature sensor whereby high membrane curvature increases FER kinase activity (Yamamoto et al., 2018). However, upon FER depletion or its kinase inhibition, we observed an impairment of Rab4-recycling endosome formation. This would result in the accumulation of recycling cargoes in sorting endosomes instead of entering recycling tubules, while transport of cargo to lysosomes would remain unaffected. Indeed, Rab4 tubule formation is an essential step for the recycling of most β1 integrins in basal breast cancer (Powelka et al., 2004; Rainero and Norman, 2013), and commitment

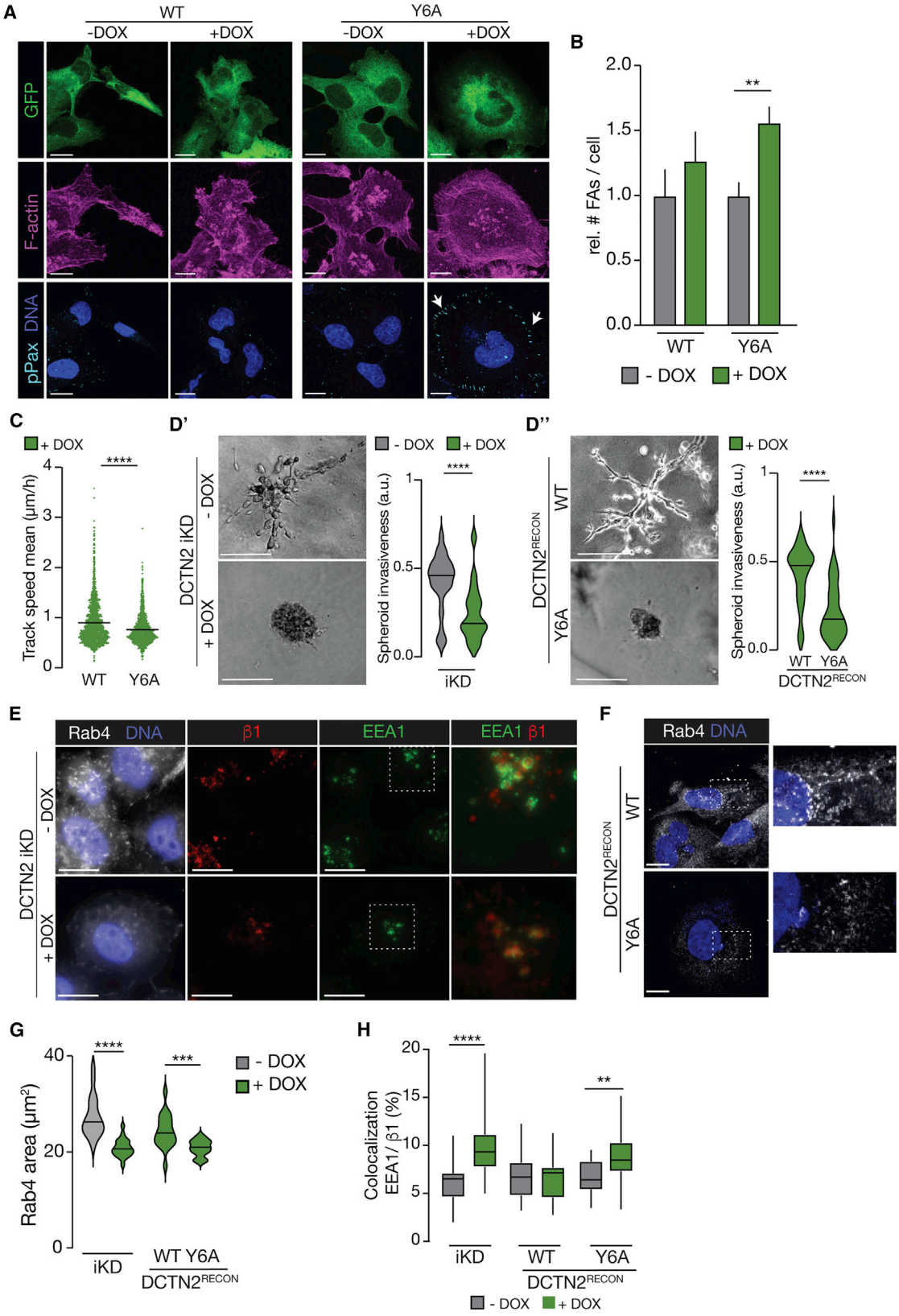

(legend on next page)

toward a fast-recycling route relies on the enrichment of specific endosomal-sorting complexes such as Rab4, retromer, and retriever in early-endosomal microdomains (Cullen and Steinberg, 2018; Sönnichsen et al., 2000). Interestingly, FER loss of function leads to an aberrant enrichment of Rab11-positive structures, which may either result from a compensatory mechanism for impaired Rab4 recycling or from another attenuation of trafficking through slow endosomal recycling.

Formation and function of endosomal compartments and sorting of cargo in the EE may involve segregation of endosomal compartments by means of a "tug of war" between dynein and a counteracting kinesin (Driskell et al., 2007). In this model, opposing motors present at the EE would either be dynamically switched on and off in a coordinated manner or maintained within a competitive balance of forces (Granger et al., 2014). Although such a mechanism is not fully understood, the interaction between Rab4 and dynein might contribute to the recruitment of dynein to control sorting of EEs (Bielli et al., 2001). Our work indicates that when DCTN2 is depleted or reconstituted by mutant DCTN2^{Y6A}, it causes an impairment in endosomal tubule formation. As such, it might suggest that modulation of the dynactin-dynein function is required for the separation of endosomal sub-domains, thus enhancing the sorting process and, consequently, tubulogenesis (Valetti et al., 1999). While the precise molecular and biochemical nature of this regulation, how FER-kinase-dependent processes control vesicular transport, and the effects on taxane responses are beyond the scope of this study, our observations suggest that tyrosine phosphorylation of DCTN2 by FER kinase is tightly regulated in a temporal and spatially restricted manner. As also proposed by others, such a multifactorial and intricate regulation of the dynein-dynactin complex could potentially control early versus late endosome formation and function (Short et al., 2002).

Notwithstanding the absence of formal evidence of *in vivo* phosphorylation of the Tyr6 residue by full-length FER, we propose that in high-curvature Rab4 endosomes, FER can phosphorylate DCTN2, leading to modulation of dynactin-dependent organelle transport complexes. Phosphorylation on DCTN2-Tyr6 would thus potentially disrupt the balance between opposing MT motors, thereby promoting tumor invasion through formation of Rab4 tubules and subsequent acceleration of adhesion and growth-receptor recycling to the plasma membrane.

In short, we have revealed DCNT2 as a potential FER kinase target in breast cancer and shown that the identified DCNT2-Tyr6 epitope affects endosomal recycling and that high FER activity is causal to both endosomal recycling and taxane responses. Because the DCTN2 Y6 residue does not impact cellular proliferation upon docetaxel treatment, our findings potentially uncouple FER-dependent growth from FER-dependent migration and invasion, whereby the latter is probably more reliant on endosomal recycling mediated by DCTN2. Our clinical data indicate that FER can predict taxane responses in a cohort of breast cancers that are all highly proliferative. We therefore hypothesize that FER—despite its control over MAPK-dependent proliferation—mostly propels migratory and metastatic cues in high-risk and basal-like breast cancers. In this context, DCTN2 may represent an intermediate regulator of these invasive processes through control of endosomal recycling. Whether this role is directly subjected to FER-dependent phosphorylation of the DCTN2 Y6 residue *in vivo* will require additional research.

Together with the prognostic value of FER expression levels in node-negative TNBC (Ivanova et al., 2013), our clinical and mechanistic studies further strengthen the importance of FER as a putative predictive biomarker and drug target in high-risk, HER2-negative breast cancer. We propose that FER expression levels should be tested prospectively as a stratifying marker for taxane-based chemotherapy in high-risk, HER2-negative breast cancers.

STAR★METHODS

Detailed methods are provided in the online version of this paper and include the following:

- KEY RESOURCES TABLE
- RESOURCE AVAILABILITY
  - Lead contact
  - Materials availability
  - Data and code availability
- EXPERIMENTAL MODEL AND SUBJECT DETAILS
  - Cell lines and culture conditions
- METHOD DETAILS
  - Plasmids
  - Virus generation and cell transduction
  - 3D morphology assessment
  - SILAC labelling - mass spectrometry
  - Thiophosphorylated peptides - mass spectrometry
  - Purification of recombinant proteins
  - Immunoprecipitation and *in vitro* kinase reactions
  - Immunoblotting analysis

Figure 7. Tyrosine 6 of DCTN2 is essential for BC cell motility and invasion

(A–C) DCTN2-Y6 controls 2D adhesion and migration. DCTN2-reconstituted cells were treated with DOX and probed for expression of pPax (cyan) and F-actin (magenta). White arrows highlight the overt presence of FA, which were quantified in (B). (C) Live fluorescence imaging was used to quantify the 2D migration speed of DOX-treated DCTN2^{RECON}-WT and DCTN2^{RECON}-Y6A cells.

(D) DCTN2 iKD (D′), DCTN^{RECON}-WT, or DCTN2^{RECON}-Y6A (D″) cells were treated with or without DOX and plated as tumor spheroids in basement membrane extract. Cells were imaged by phase contrast, and tumor spheroid invasiveness was quantified. Scale bars, 50 μm.

(E–H) The DCTN2 tyrosine 6 residue is necessary for endosomal recycling. DCTN2 iKD cells were treated with or without DOX and stained for Rab4 (gray), β1-integrin (red), and EEA1 (green) (E). DCTN2^{RECON}-WT or DCTN2^{RECON}-Y6A cells were treated with DOX and stained for Rab4 (gray). Scale bars, 15 μm (F). Quantifications of Rab4-positive vesicle areas are shown in (G). Co-localization studies for β1-integrin and EEA1 in DCTN2 iKD, DCTN2^{RECON}-WT, and DCTN2^{RECON}-Y6A cells treated with or without DOX (H).

Error bars indicate SD; $^{**}p < 0.01$, $^{***}p < 0.001$, and $^{****}p < 0.0001$. Statistical significance was calculated using one-way ANOVA.

See also Figure S6.

- Immunofluorescence analysis
- Live cell imaging
- BSA/Transferrin uptake assay
- Cell counting and cell cycle profiling
- Colony formation assays
- Clinical data analyses

- QUANTIFICATION AND STATISTICAL ANALYSIS
  - Quantification of colocalization assays
  - 3D morphology quantification
  - Analysis of live cell imaging data
  - Quantification of immunofluorescence
  - Quantifications of Rab4- and Rab11-positive vesicle areas
  - Mass spectrometry
  - Statistical analysis

SUPPLEMENTAL INFORMATION

Supplemental information can be found online at https://doi.org/10.1016/j.celrep.2022.110584.

ACKNOWLEDGMENTS

We thank N. Bovenschen, M. Hadders, B. Levin, K. Shokat, R. Schackmann, I. Ivanova, and S. Boogaard for the experimental support. Also, we thank the Dutch Breast Cancer Research Group (BOOG) for providing clinical data from the BOOG 2005-02 MATADOR study. This research was supported by KWF Kankerbestrijding (UU2014-7201), the Dutch Research Council TOP grant (NWO-TOP 02007), and the European Union's Horizon 2020 FET Proactive program under grant agreement no. 731957 (MECHANO-CONTROL).

AUTHOR CONTRIBUTIONS

Conceptualization, S.T. and P.W.B.D.; methodology, S.T., S.M.A.L., and P.W.B.D.; investigation, S.T., N.L., M.P., M.O., M.S., L.M.S., R.C.C.H., P.W.B.D., and R.v.E.; formal analysis, S.T., N.L., M.P., M.O., M.A.K.R., M.S., L.M.S., R.C.C.H., E.v.W., H.V., and H.R.; resources, H.M.O. and B.M.T.B.; writing – original draft, S.T.; writing – review & editing, S.T., P.W.B.D., S.M.A.L., J.K., and S.C.L.; funding acquisition, P.W.B.D.; supervision, P.W.B.D.

DECLARATION OF INTERESTS

S.C.L. and H.M.O. received funding from Amgen, Sanofi, and the Dutch Cancer Society during the conduct of the study. S.C.L. reports grants and nonfinancial support from AstraZeneca, Genentech/Roche, Tesaro, and Immunomedics. S.C.L. received funding from Eurocept Pharmaceuticals, Novartis, and Pfizer and other support from Cergentis, IBM, Daiichi Sankyo, and Bayer outside the submitted work. S.C.L. is an advisory board member for Cergentis, IBM, Novartis, Pfizer, Roche, and Sanofi. H.M.O. is an advisory board member for Roche, Novartis, Pfizer, and MSD. J.K. received funding from Genentech/Roche. All other authors declare no competing interests.

Received: April 12, 2021
Revised: October 28, 2021
Accepted: March 7, 2022
Published: April 5, 2022

REFERENCES

Ahn, J., Truesdell, P., Meens, J., Kadish, C., Yang, X., Boag, A.H., and Craig, A.W.B. (2013). Fer protein-tyrosine kinase promotes lung adenocarcinoma cell invasion and tumor metastasis. Mol. Cancer Res. *11*, 952–963. https://doi.org/10.1158/1541-7786.mcr-13-0003-t.

Arregui, C., Pathre, P., Lilien, J., and Balsamo, J. (2000). The nonreceptor tyrosine kinase fer mediates cross-talk between N-cadherin and beta1-integrins. J. Cell Biol. *149*, 1263–1274.

Bielli, A., Thörnqvist, P.O., Hendrick, A.G., Finn, R., Fitzgerald, K., and McCaffrey, M.W. (2001). The small GTPase Rab4A interacts with the central region of cytoplasmic dynein light intermediate chain-1. Biochem. Biophysical Res. Commun. *281*, 1141–1153. https://doi.org/10.1006/bbrc.2001.4468.

Bishop, A.C., Ubersax, J.A., Petsch, D.T., Matheos, D.P., Gray, N.S., Blethrow, J., Shimizu, E., Tsien, J.Z., Schultz, P.G., Rose, M.D., et al. (2000). A chemical switch for inhibitor-sensitive alleles of any protein kinase. Nature *407*, 395–401. https://doi.org/10.1038/35030148.

Blethrow, J.D., Glavy, J.S., Morgan, D.O., and Shokat, K.M. (2008). Covalent capture of kinase-specific phosphopeptides reveals Cdk1-cyclin B substrates. Proc. Natl. Acad. Sci. U S A *105*, 1442–1447. https://doi.org/10.1073/pnas.0708966105.

Borten, M.A., Bajikar, S.S., Sasaki, N., Clevers, H., and Janes, K.A. (2018). Automated brightfield morphometry of 3D organoid populations by OrganoSeg. Scientific Rep. *8*, 5319. https://doi.org/10.1038/s41598-017-18815-8.

Cardoso, F., Paluch-Shimon, S., Senkus, E., Curigliano, G., Aapro, M.S., André, F., Barrios, C.H., Bergh, J., Bhattacharyya, G.S., Biganzoli, L., et al. (2020). 5th ESO-ESMO international consensus guidelines for advanced breast cancer (ABC 5). Ann. Oncol. *31*, 1623–1649.

Caviston, J.P., and Holzbaur, E.L.F. (2006). Microtubule motors at the intersection of trafficking and transport. Trends Cell Biol. *16*, 530–537. https://doi.org/10.1016/j.tcb.2006.08.002.

Chen, Y., Aardema, J., and Corey, S.J. (2013). Biochemical and functional significance of F-BAR domain proteins interaction with WASP/N-WASP. Semin. Cell Dev. Biol. *24*, 280–286. https://doi.org/10.1016/j.semcdb.2013.01.005.

Cullen, P.J., and Steinberg, F. (2018). To degrade or not to degrade: mechanisms and significance of endocytic recycling. Nat. Rev. Mol. Cell Biol. *19*, 679–696. https://doi.org/10.1038/s41580-018-0053-7.

Delevoye, C., Heiligenstein, X., Ripoll, L., Gilles-Marsens, F., Dennis, M.K., Linares, R.A., Derman, L., Gokhale, A., Morel, E., Faundez, V., et al. (2016). BLOC-1 brings together the actin and microtubule cytoskeletons to generate recycling endosomes. Curr. Biol. *26*, 1–13. https://doi.org/10.1016/j.cub.2015.11.020.

Driskell, O.J., Mironov, A., Allan, V.J., and Woodman, P.G. (2007). Dynein is required for receptor sorting and the morphogenesis of early endosomes. Nat. Cell Biol. *9*, 113–120. https://doi.org/10.1038/ncb1525.

Eden, E.R., White, I.J., Tsapara, A., and Futter, C.E. (2010). Membrane contacts between endosomes and ER provide sites for PTP1B–epidermal growth factor receptor interaction. Nat. Cell Biol. *12*, 267–272. https://doi.org/10.1038/ncb2026.

Filippakopoulos, P., Kofler, M., Hantschel, O., Gish, G.D., Grebien, F., Salah, E., Neudecker, P., Kay, L.E., Turk, B.E., Superti-Furga, G., et al. (2008). Structural coupling of SH2-kinase domains links Fes and Abl substrate recognition and kinase activation. Cell *134*, 793–803. https://doi.org/10.1016/j.cell.2008.07.047.

Granger, E., McNee, G., Allan, V., and Woodman, P. (2014). The role of the cytoskeleton and molecular motors in endosomal dynamics. Semin. Cell Dev. Biol. *31*, 20–29. https://doi.org/10.1016/j.semcdb.2014.04.011.

Greer, P. (2002). Closing in on the biological functions of Fps/Fes and Fer. Nat. Rev. Mol. Cell Biol. *3*, 278–289. https://doi.org/10.1038/nrm783.

Guo, C., and Stark, G.R. (2011). FER tyrosine kinase (FER) overexpression mediates resistance to quinacrine through EGF-dependent activation of NF-kappaB. Proc. Natl. Acad. Sci. U S A. *108*, 7968–7973. https://doi.org/10.1073/pnas.1105369108.

Hertz, N.T., Wang, B.T., Allen, J.J., Zhang, C., Dar, A.C., Burlingame, A.L., and Shokat, K.M. (2010). Chemical genetic approach for kinase-substrate mapping by covalent capture of thiophosphopeptides and analysis by mass spectrometry. Curr. Protoc. Chem. Biol. *2*, 15–36. https://doi.org/10.1002/9780470559277.ch090201.

Hikri, E., Shpungin, S., and Nir, U. (2009). Hsp90 and a tyrosine embedded in the Hsp90 recognition loop are required for the Fer tyrosine kinase activity. Cell Signal. *21*, 588–596. https://doi.org/10.1016/j.cellsig.2008.12.011.

Homma, N., Takei, Y., Tanaka, Y., Nakata, T., Terada, S., Kikkawa, M., Noda, Y., and Hirokawa, N. (2003). Kinesin superfamily protein 2A (KIF2A) functions in suppression of collateral branch extension. Cell *114*, 229–239. https://doi.org/10.1016/s0092-8674(03)00522-1.

Humphrey, S.J., Azimifar, S.B., and Mann, M. (2015). High-throughput phosphoproteomics reveals in vivo insulin signaling dynamics. Nat. Biotechnol. *33*, 990–995. https://doi.org/10.1038/nbt.3327.

Ivanova, I.A., Vermeulen, J.F., Ercan, C., Houthuijzen, J.M., Saig, F.A., Vlug, E.J., van der Wall, E., van Diest, P.J., Vooijs, M., and Derksen, P.W. (2013). FER kinase promotes breast cancer metastasis by regulating alpha6- and beta1-integrin-dependent cell adhesion and anoikis resistance. Oncogene *32*, 5582–5592. https://doi.org/10.1038/onc.2013.277.

Katrukha, E. (2020). Ekatrukha/ComDet: ComDet 0.5.3 (0.5.3) [Computer Software] (Zenodo). https://doi.org/10.5281/zenodo.4281064.

Kim, L., and Wong, T.W. (1995). The cytoplasmic tyrosine kinase FER is associated with the catenin-like substrate pp120 and is activated by growth factors. Mol. Cell Biol. *15*, 4553–4561.

Kim, L., and Wong, T.W. (1998). Growth factor-dependent phosphorylation of the actin-binding protein cortactin is mediated by the cytoplasmic tyrosine kinase FER. J. Biol. Chem. *273*, 23542–23548.

Li, H., Ren, Z., Kang, X., Zhang, L., Li, X., Wang, Y., Xue, T., Shen, Y., and Liu, Y. (2009). Identification of tyrosine-phosphorylated proteins associated with metastasis and functional analysis of FER in human hepatocellular carcinoma cells. BMC Cancer *9*, 366. https://doi.org/10.1186/1471-2407-9-366.

Liu, J.J. (2017). Regulation of dynein-dynactin-driven vesicular transport. Traffic *18*, 336–347. https://doi.org/10.1111/tra.12475.

Liu, S., Xiong, X., Zhao, X., Yang, X., and Wang, H. (2015). F-BAR family proteins, emerging regulators for cell membrane dynamic changes-from structure to human diseases. J. Hematol. Oncol. *8*, 47. https://doi.org/10.1186/s13045-015-0144-2.

Lonic, A., Gehling, F., Belle, L., Li, X., Schieber, N.L., Nguyen, E.V., Goodall, G.J., Parton, R.G., Daly, R.J., and Khew-Goodall, Y. (2021). Phosphorylation of PKCδ by FER tips the balance from EGFR degradation to recycling. J. Cell Biol. *220*, e201902073. https://doi.org/10.1083/jcb.201902073.

Matsuura, Y. (2019). High-resolution structural analysis shows how different crystallographic environments can induce alternative modes of binding of a phosphotyrosine peptide to the SH2 domain of Fer tyrosine kinase. Protein Sci. *28*, 2011–2019. https://doi.org/10.1002/pro.3713.

McCaffrey, M.W., Bielli, A., Cantalupo, G., Mora, S., Roberti, V., Santillo, M., Drummond, F., and Bucci, C. (2001). Rab4 affects both recycling and degradative endosomal trafficking. FEBS Lett *495*, 21–30.

Oneyama, C., Yoshikawa, Y., Ninomiya, Y., Iino, T., Tsukita, S., and Okada, M. (2016). Fer tyrosine kinase oligomer mediates and amplifies Src-induced tumor progression. Oncogene *35*, 501–512. https://doi.org/10.1038/onc.2015.110.

Perez-Riverol, Y., Csordas, A., Bai, J., Bernal-Llinares, M., Hewapathirana, S., Kundu, D.J., Inuganti, A., Griss, J., Mayer, G., Eisenacher, M., et al. (2019). The PRIDE database and related tools and resources in 2019: improving support for quantification data. Nucleic Acids Res. *47*, D442–D450. https://doi.org/10.1093/nar/gky1106.

Powelka, A.M., Sun, J., Li, J., Gao, M., Shaw, L.M., Sonnenberg, A., and Hsu, V.W. (2004). Stimulation-dependent recycling of integrin beta1 regulated by ARF6 and Rab11. Traffic *5*, 20–36. https://doi.org/10.1111/j.1600-0854.2004.00150.x.

Rafn, B., and Kallunki, T. (2012). A way to invade: a story of ErbB2 and lysosomes. Cell Cycle *11*, 2415–2416. https://doi.org/10.4161/cc.20860.

Rainero, E., and Norman, J.C. (2013). Late endosomal and lysosomal trafficking during integrin-mediated cell migration and invasion. BioEssays *35*, 523–532. https://doi.org/10.1002/bies.201200160.

Rapley, J., Nicolàs, M., Groen, A., Regué, L., Bertran, M.T., Caelles, C., Avruch, J., and Roig, J. (2008). The NIMA-family kinase Nek6 phosphorylates the kinesin Eg5 at a novel site necessary for mitotic spindle formation. J. Cell Sci. *121* (*Pt 23*), 3912–3921. https://doi.org/10.1242/jcs.035360.

van Rossum, A.G.J., Kok, M., van Werkhoven, E., Opdam, M., Mandjes, I.A.M., van Leeuwen-Stok, A.E., van Tinteren, H., Imholz, A.L.T., Portielje, J.E.A., Bos, M.M.E.M., et al. (2018). Adjuvant dose-dense doxorubicin-cyclophosphamide versus docetaxel-doxorubicin-cyclophosphamide for high-risk breast cancer: first results of the randomised MATADOR trial (BOOG 2004-04). Eur. J. Cancer *102*, 40–48. https://doi.org/10.1016/j.ejca.2018.07.013.

Sangrar, W., Gao, Y., Scott, M., Truesdell, P., and Greer, P.A. (2007). Fer-mediated cortactin phosphorylation is associated with efficient fibroblast migration and is dependent on reactive oxygen species generation during integrin-mediated cell adhesion. Mol. Cell Biol. *27*, 6140–6152. https://doi.org/10.1128/mcb.01744-06.

Schackmann, R.C., Amersfoort, M. van, Haarhuis, J.H., Vlug, E.J., Halim, V.A., Roodhart, J.M., Vermaat, J.S., Voest, E.E., Groep, P. van der, Diest, P. J. van, et al. (2011). Cytosolic p120-catenin regulates growth of metastatic lobular carcinoma through Rock1-mediated anoikis resistance. J. Clin. Invest. *121*, 3176–3188. https://doi.org/10.1172/jci41695.

Schindelin, J., Arganda-Carreras, I., Frise, E., Kaynig, V., Longair, M., Pietzsch, T., Preibisch, S., Rueden, C., Saalfeld, S., Schmid, B., et al. (2012). Fiji: an open-source platform for biological-image analysis. Nat. Methods *9*, 676–682. https://doi.org/10.1038/nmeth.2019.

Schneider, C.A., Rasband, W.S., and Eliceiri, K.W. (2012). NIH Image to ImageJ: 25 years of image analysis. Nat. Methods *9*, 671–675. https://doi.org/10.1038/nmeth.2089.

Shapovalova, Z., Tabunshchyk, K., and Greer, P.A. (2007). The Fer tyrosine kinase regulates an axon retraction response to Semaphorin 3A in dorsal root ganglion neurons. BMC Dev. Biol. *7*, 133. https://doi.org/10.1186/1471-213x-7-133.

Short, B., Preisinger, C., Schaletzky, J., Kopajtich, R., and Barr, F.A. (2002). The Rab6 GTPase regulates recruitment of the dynactin complex to Golgi membranes. Curr. Biol. *12*, 1792–1795. https://doi.org/10.1016/s0960-9822(02)01221-6.

van der Sluijs, P., Hull, M., Webster, P., Mâle, P., Goud, B., and Mellman, I. (1992). The small GTP-binding protein rab4 controls an early sorting event on the endocytic pathway. Cell *70*, 729–740. https://doi.org/10.1016/0092-8674(92)90307-x.

Sonnenberg, A., Janssen, H., Hogervorst, F., Calafat, J., and Hilgers, J. (1987). A complex of platelet glycoproteins Ic and IIa identified by a rat monoclonal antibody. J. Biol. Chem. *262*, 10376–10383.

Sönnichsen, B., Renzis, S.D., Nielsen, E., Rietdorf, J., and Zerial, M. (2000). Distinct membrane domains on endosomes in the recycling pathway visualized by multicolor imaging of Rab4, Rab5, and Rab11. J. Cell Biol. *149*, 901–914. https://doi.org/10.1083/jcb.149.4.901.

Tavares, S., Vieira, A.F., Taubenberger, A.V., Araújo, M., Martins, N.P., Brás-Pereira, C., Polónia, A., Herbig, M., Barreto, C., Otto, O., et al. (2017). Actin stress fiber organization promotes cell stiffening and proliferation of pre-invasive breast cancer cells. Nat. Commun. *8*, 15237. https://doi.org/10.1038/ncomms15237.

Thomas, C., and Gustafsson, J.A. (2011). The different roles of ER subtypes in cancer biology and therapy. Nat. Rev. Cancer *11*, 597–608. https://doi.org/10.1038/nrc3093.

Tinevez, J.-Y., Perry, N., Schindelin, J., Hoopes, G.M., Reynolds, G.D., Laplantine, E., Bednarek, S.Y., Shorte, S.L., and Eliceiri, K.W. (2017). TrackMate: an open and extensible platform for single-particle tracking. Methods *115*, 80–90. https://doi.org/10.1016/j.ymeth.2016.09.016.

Ullrich, O., Reinsch, S., Urbé, S., Zerial, M., and Parton, R.G. (1996). Rab11 regulates recycling through the pericentriolar recycling endosome. J. Cell Biol. *135*, 913–924. https://doi.org/10.1083/jcb.135.4.913.

Valetti, C., Wetzel, D.M., Schrader, M., Hasbani, M.J., Gill, S.R., Kreis, T.E., and Schroer, T.A. (1999). Role of dynactin in endocytic traffic: effects of

dynamitin overexpression and colocalization with CLIP-170. Mol. Biol. Cell *10*, 4107–4120. https://doi.org/10.1091/mbc.10.12.4107.

Vaughan, P.S., Leszyk, J.D., and Vaughan, K.T. (2001). Cytoplasmic dynein intermediate chain phosphorylation regulates binding to dynactin. J. Biol. Chem. *276*, 26171–26179. https://doi.org/10.1074/jbc.m102649200.

van de Ven, R.A.H., Tenhagen, M., Meuleman, W., van Riel, J.J.G., Schackmann, R.C.J., and Derksen, P.W.B. (2015). Nuclear p120-catenin regulates the anoikis resistance of mouse lobular breast cancer cells through Kaiso-dependent Wnt11 expression. Dis. Models Mech. *8*, 373–384. https://doi.org/10.1242/dmm.018648.

Yamamoto, H., Kondo, A., and Itoh, T. (2018). A curvature-dependent membrane binding by tyrosine kinase Fer involves an intrinsically disordered region. Biochem. Biophysical Res. Commun. *495*, 1522–1527. https://doi.org/10.1016/j.bbrc.2017.12.009.

Zirngibl, R., Schulze, D., Mirski, S.E., Cole, S.P., and Greer, P.A. (2001). Subcellular localization analysis of the closely related Fps/Fes and Fer protein-tyrosine kinases suggests a distinct role for Fps/Fes in vesicular trafficking. Exp. Cell Res. *266*, 87–94. https://doi.org/10.1006/excr.2001.5217.

STAR★METHODS

KEY RESOURCES TABLE

REAGENT or RESOURCE	SOURCE	IDENTIFIER
Antibodies		
phospho-p44/42 MAPK	Cell Signaling	Cat# 9101s; RRID: AB_331646
mouse anti-FER	Cell Signaling	Cat# 4268s; RRID: AB_2278286
rabbit anti-GAPDH	Millipore	Cat# Mab374; RRID: AB_2107445
mouse anti-thiophosphate ester	Abcam	Cat# ab92570; RRID: AB_10562142
rabbit anti-V5	Cell Signaling	Cat# 13202; RRID: AB_2687461
mouse anti-p44/42 MAPK	Cell Signaling	Cat# 9107; RRID: AB_10695739
mouse anti-phospho tyrosine	BD Transduction	Cat# 610000; RRID: AB_397423
mouse anti-DCTN2	Santa Cruz Biotechnology	Cat# sc-393389; RRID: AB_2909607
HRP-conjugated goat anti-mouse	Bio-rad	Cat# 170-6516; RRID: AB_11125547
HRP-conjugated goat anti-rabbit	Bio-rad	Cat# 170-6515; RRID: AB_11125142
IRDy680 labeled goat anti-rabbit	Li-Cor	Cat# 92668071; RRID: AB_10956166
IRDye800 labeled goat anti-mouse	Li-Cor	Cat# 92632210; RRID: AB_621842
mouse anti-GST	Santa Cruz Biotechnology	Cat# sc-138; RRID: AB_627677
anti-phospho Paxillin	Life Technologies	Cat# 44722G; RRID: AB_2533733
mouse anti-alpha-tubulin	Sigma-Aldrich	Cat# T5168; RRID: AB_477579
mouse anti-LAMP1	Thermo Fisher Scientific	Cat# MA1-164; RRID: AB_2536869
rat anti-β1 Integrin	Developmental Studies Hybridoma Bank	Cat# 528306; RRID: AB_528306
rat anti-a6 Integrin	It was a kind gift from Dr. Sonnenberg	N/A
mouse anti-Rab4b	Santa Cruz Biotechnology	Cat# 271982; RRID: AB_10709179
rabbit anti-Rab11	Thermofisher	Cat# 71-5300; RRID: AB_87868
rabbit anti-DCTN2	Sigma Aldrich	Cat# HPA039715; RRID: AB_10795154
Ki-67	Dako	Cat# M7240; RRID: AB_2142367
rat anti-tyrosinated α-tubulin	Thermo Fisher Scientific	Cat# MA1-80017; RRID: AB_2210201
rabbit anti-de-tyrosinated αTubulin	Abcam	Cat# ab48389; RRID: AB_869990
rabbit anti-CAMSAP2	Novus	Cat# NBP1-21402; RRID: AB_2068823
Bacterial and virus strains		
E. coli Rosetta2(DE3)	Novagen	Cat# 71400
Chemicals, peptides, and recombinant proteins		
NM-PP1	Calbiochem	Cat# 529581
Cultrex Basement Membrane Extract	Trevigen	Cat# 3533-005-02
cOmplete , EDTA-free Protease Inhibitor Cocktail Roche	Roche Applied Science	Cat# 4693116001
GST-Tubulin	Sigma	Cat# SRP5148
ATPgS	BioLog	Cat# A 060-05
N6-furfuryl(Fu)-ATPgS	BioLog	Cat# F 008-05
N6-phenylethyl(Phe)-ATPgS	BioLog	Cat# P 026-05
N6-benzyl(Bn)-ATPgS	BioLog	Cat# B 072-05
p-nitrobenzyl mesylate	Abcam	Cat# ab138910
Doxycycline	Sigma	Cat# D9891-1G
SiR-Lysosome	Tebu-bio	Cat# SC012
with BSA-Alexa555	Invitrogen	Cat# A34786
Transferrin-Alexa647	Invitrogen	Cat# T23366
Purified GST-FER WT protein	This study	N/A
Purified GST-FER AS protein	This study	N/A

(*Continued on next page*)

Continued

REAGENT or RESOURCE	SOURCE	IDENTIFIER
Purified GST- FER-D742R protein	This study	N/A
Purified GST- MAPK1 protein	This study	N/A
Purified GST- DCTN2 protein	This study	N/A
Dithiothreitol	Sigma	Cat# R0861
Doxycycline free FCS	Hyclone GE Healthcare	Cat# SH30070.03T
penicillin and streptomycin	Sigma	Cat# P0781-100ML
DMSO	Sigma	Cat# D5879-1L
TCEP	Sigma-Aldrich	Cat# 646547-10X1ml
HEPES	Sigma	Cat# H3375-25G
Triton X-100	Sigma	Cat# T9284
NaCl	Sigma	Cat# 71376-1KG
NaVO3	Sigma	Cat# S6508-10G
NaF	Sigma	Cat# S6776-100G
NP-40	Merck	Cat# 492016-100ML
Urea	Ambion	Cat# AM9902
ammonium bicarbonate	Sigma	Cat# 09830-1kg
Tween-20	VWR International	Cat# 8.22184.0500
ECL-HRP detection kit	Advanstra	Cat# K-12045-D20
ProLong antifade	Molecular Probes	Cat# P36961
Docetaxel	Accord	N/A
Paclitaxel	Enzo Life Sciences	Cat# BML-T140
GFP-Trap anti-GFP beads	Chromotek	Cat# gta-20
Critical commercial assays		
QuickChange	Agilent Technologies	Cat# 200521
in-fusion HD enzyme	Takara	Cat# 639649
CloneJET PCR Cloning Kit	Thermo Fischer scientific	Cat# K1231
GATEWAY cloning	Thermo Fischer scientific	Cat# 11791019
Deposited data		
The mass spectrometry proteomics data	ProteomeXchange Consortium via the PRIDE partner repository	PRIDE: PXD021307
The bulk mRNA sequencing data	GEO (https://www.ncbi.nlm.nih.gov/geo/query/acc.cgi?acc=GSE167977)	Cat# GSE167977
Experimental models: Cell lines		
Human - MDA-MB-231	Eppelheim	N/A
Human - HEK293T	N/A	N/A
Oligonucleotides		
N/A	See Table S2 for full list of oligonucleotide sequences	N/A
Recombinant DNA		
pAcG2T vector	Addgene	Cat# 38167
Plasmid pGEX-6P-1	GE Healthcare	Cat# 28-9546-48
pLV_FUTG_Tet_Inducible_shRNA	This study	N/A
pDONR201	Invitrogen	Cat# 12536017
pENTRY-DCTN2WT	This study	N/A
pENTRY-DCTN2Y6A	This study	N/A
pJET-DCTN2WT	This study	N/A
pLV.CMV.GFP-DCTN2WT	This study	N/A
pLV.CMV.GFP-DCTN2Y6A	This study	N/A

(*Continued on next page*)

Continued

REAGENT or RESOURCE	SOURCE	IDENTIFIER
Software and algorithms		
ImageJ	Schneider et al., 2012	https://imagej.nih.gov/ij/
R version 3.6.1, package tableone 0.1.11	N/A	https://cran.r-project.org/
R Packages survival 3.1.11, survminer 0.4.6	N/A	https://cran.r-project.org/
OrganoSeg	Borten et al., 2018	N/A
Imaris for Tracking software	Bitplane, Oxford Instruments	N/A
Fiji TrackMate plugin	Tinevez et al., 2017	https://doi.org/10.1016/j.ymeth.2016.09.016
Volocity	Quorum Technologies	
Fiji Comdet plugin	Katrukha, 2020	https://github.com/ekatrukha/ComDet
Graphpad Prism	Graphpad	https://www.graphpad.com/scientificsoftware/prism/

RESOURCE AVAILABILITY

Lead contact

Information and requests for resources and reagents should be directed to and will be fulfilled by the Lead Contact, Patrick W. B. Derksen (P.W.B.Derksen@umcutrecht.nl).

Materials availability

Plasmids and cell lines generated in this study can be obtained through the Lead Contact.

Data and code availability

- The MS proteomics data have been deposited to the ProteomeXchange Consortium via the PRIDE (Perez-Riverol et al., 2019) partner repository with the dataset identifier PRIDE: PXD021307. Dataset will be made available as of the date of publication.
- This paper does not report original code.
- Any additional information required to reanalyze the data reported in this work is available from the Lead Contact upon request.

EXPERIMENTAL MODEL AND SUBJECT DETAILS

Cell lines and culture conditions

MDA-MB-231 cells (MM231) were provided by Cell Lines Service (Eppelheim, Germany). STR typing of all cell lines was verified by PCR. Sub-confluent cells were treated with 3.9 nM doxycycline (DOX) for at least 5 days. FER^{RECON} cells were subsequently, treated with 1 μM NM-PP1 (Calbiochem, 529581) or DMSO for 72h.

For 3D assays, MM231 cells were added to Cultrex Basement Membrane Extract (BME) (Trevigen; 3533-005-02) at a density of 1000 cells/50 μL BME. Droplets of 50 μL were added to flat bottom optical plastic 24-well plates (Corning, Tewksbury, USA). Plates were incubated for 45 min. at 37°C to allow the BME to solidify, after which 500 μL normal growth medium was added. Cells were cultured for 7 days at 37°C.

METHOD DETAILS

Plasmids

FER M637A was generated by site-directed mutagenesis (200521, QuickChange; Agilent Technologies, Wilmington DE) using GST-FER WT in pAcG2T vector (38167, Addgene) as template. FER truncated forms, DCTN2 and MAPK1 were excised from pJET vectors using *EcoR*I and *Not*I and ligated into the pGEX-6P-1 vector to introduce the GST tag. Full length FER-AS (M637A FER) cDNA resistant to FER shRNA expressed by MDA-MB-231 FER-iKD [980-998] (MM231 FER-iKD) was generated by introducing four silent mutations in the target sequence, by site-directed mutagenesis. Inducible DCTN2-specific shRNA constructs (DCTN2-iKD) were generated using two shRNA oligo nucleotides (flanked by *Xho*I and *Age*I restriction sites). shRNA oligonucleotides were annealed and ligated in pLV_FUTG_Tet_Inducible_shRNA using in-fusion HD enzyme (639649, Takara).

pENTRY-$DCTN2^{WT}$ and pENTRY-$DCTN2^{Y6A}$ were generated using GATEWAY cloning (Thermo Fischer scientific) as follows: pJET-$DCTN2^{WT}$ vector was used as template to generate $DCTN2^{WT}$ PCR products flanked by *att*B recombination sites.

pENTRY-DCTN2^{Y6A} was generated by site-directed mutagenesis (200521, QuikChange; Agilent Technologies, Wilmington DE) of pJET-DCTN2^{WT}. The *att*B sites were generated using pJET-DCTN2^{Y6A} vector as template. We cloned DCNT2^{WT} and DCTN2^{Y6A} into a pDONR201 using a BP Reaction, generating pENTRY-DCTN2^{WT} and pENTRY-DCTN2^{Y6A}. Full length DCTN2^{WT} and DCTN2^{Y6A} cDNAs resistant to DCTN2 shRNA 2 were generated by introducing three silent mutations in pENTRY-DCTN2^{WT} and pENTRY-DCTN2^{Y6A}. pLV.CMV.GFP-DCTN2^{WT} and pLV.CMV.GFP-DCTN2^{Y6A} were constructed using GATEWAY cloning. All constructs were verified by DNA sequencing.

Sequences of oligonucleotides are detailed in Table S3.

Virus generation and cell transduction

Inducible shRNA (iKD) constructs targeting DCTN2, and DCTN2^{WT}, DCTN2^{Y6A} and FER-AS-expressing lentivirus production and transduction have been described previously (Schackmann et al., 2011) In short, lentiviral particles were produced in HEK293T or COS7 cells using third-generation packaging constructs. Supernatant containing viral particles was harvested 48 hours after transfection, passed through a 45μm filter, and concentrated 10 to 150-fold by ultra-centrifugation (175,000g; 150 minutes). MM231 cells were transduced overnight in the presence of 4 μg/mL polybrene (Sigma-Aldrich). DOX-inducible cell lines were treated for 4 days with 0.1 μg/mL DOX, refreshed every 2 days.

3D morphology assessment

Brightfield images were acquired by using a 10× objective on an EVOS M5000 Imaging System. Images were white balanced (after preliminary autoexposure). At least 5 images were acquired per chamber well, and at least two wells were imaged per condition. Three independent experiments were performed.

SILAC labelling - mass spectrometry

For SILAC labelling, MM231 FER-iKD cells were grown in DMEM medium for SILAC (88364, Invitrogen), containing heavy (13C6- and 15N2-lysine) or light (12C- and 14N-lysine) amino acids (Dundee Cell Products). After 8-10 passages, incorporation of the labeled amino acids was tested by LC/MS/MS. Control cells were cultured in ''light'' and DOX-treated cells in ''heavy'' medium (forward experiment). As a control, control cells were cultured in ''heavy'' and DOX-treated cells in ''light'' medium (reverse experiment). At 80–90% confluence, cells were harvested and lysed with lysis buffer containing 8M Urea, 1M ammonium bicarbonate (ABC)-buffer (non-TMT labeling), phosphatase inhibitor cocktail 2 and 3 (Roche), protease inhibitor cocktail (Roche), 10mM 10 mM tris(2-carboxyethyl)-phosphine (TCEP), 40mM 2-chloroacetamide (CAA). The number of cells was quantified, and cell extracts from each cell line were mixed at a 1:1 ratio. Samples were processed as previously described (Humphrey et al., 2015). Briefly, the samples harvested in lysis buffer were sonicated followed by overnight digestion. After digestion the samples were concentrated and cleaned up using Sep-Pak C18 columns. The samples were enriched for phosphopeptides. First the samples were eluted from Sep-Pak column using 1 ml Buffer (80% acetonitrile and 0.1% formic acid) and acidified by adding Trifluoroacetic acid (TFA) to 6% concentration. The samples were then added to pre-washed TiO2 beads (∼ 10:1 beads:protein; ZirChrom Sachtopore-NP, 5um, 300A) and incubated for 5 min at 37C on a shaker. The supernatant was then incubated again on a second batch of TiO2 beads. Phosphopeptides were now bound to the TiO2 beads. After incubation the beads were centrifuged and the supernatant was removed. The beads were then washed 3 times with wash buffer (60% Acetonitrile, 1% TFA) using centrifugation to remove remaining non-phosphopeptides. The samples were then transferred with transfer buffer (80% Acetonitrile, 0.5% Formic Acid) to a stagetip with a single C8 layer. The samples were centrifuged to complete dryness and eluted with elution buffer (40% acetonitrile, 60% NH4OH (25% HPLC grade) in a new container. After elution the samples were concentrated and cleaned up on C18 stagetips. The samples were then eluted and fractioned using Reverse Phase high pH OnStagetip Fractionation into 3 fractions. After elution the samples were concentrated to dryness by SpeedVac and resuspended with 14 ul Buffer (water, 0.1% formic acid) half of which is used for mass-spec analysis. The samples were then analysed on an Orbitrap Fusion^{TM} Tribrid^{TM} mass spectrometer using a 240-minute gradient, full scan resolution of 240k, cycle time of 1 second and HCD fragmentation readout in the Ion Trap on rapid scanout. Three independent experiments were performed. The MS proteomics data have been deposited to the ProteomeXchange Consortium via the PRIDE (Perez-Riverol et al., 2019) partner repository with the dataset identifier PXD021307.

Thiophosphorylated peptides - mass spectrometry

Covalent capture of thio-phosphorylated substrate proteins was performed using 2 mg protein from lysates labeled with bulky ATPγs. Isolation of the resulting phospho-peptides and analysis by LC-MC/MS was performed as previously described (Blethrow et al., 2008). Cells were lysed with complete denaturation buffer (8M Urea, 10 mM TCEP, 100 mM NH_4HCO_3, 2 mM EDTA). Denaturation buffer was added to the labeled lysate such that the final concentration is 6 M Urea, followed by 1 hour incubation at 55°C. Sample was diluted by adding 50 mM NH_4HCO_3 such that the final concentration of Urea was 2 M, and added 1 M TCEP to a final concentration of 10 mM and trypsin in a 1:50-1:10 ratio. After an incubation at 37°C for overnight, the sample was acidified by the addition of 2.5% TFA to attain 0.1% TFA. C-18 Sep Pak were washed with 0.1% TFA 50% Acetonitrile:H_2O, followed by 10 mL of 0.1% TFA:H_2O and the acidified sample was loaded to the column. Then, the column was washed with 0.1% TFA:H_2O. Peptides were eluted with 1 mL 0.1% TFA in 50% Acetonitrile:H_2O and concentrated to near dryness using a speed vacuum.

Iodoacetyl agarose beads were prepared for each sample by pipeting 50% resin slurry into a siliconized tube. After a short spin at 10,000*g* followed by supernatant removal, beads were washed with 200 mM HEPES pH 7.0. A blocking solution of 50% Acetonitrile 50% 20 mM HEPES pH 7.0 and 5 mg/mL BSA was added to the beads and incubated for ten minutes in the dark. Additionally, we prepared another covalent capture reaction by directly adding several pmols of the thio-phosphorylated CREB peptide to the beads in 50% Acetonitrile 50% 20 mM HEPES pH 7.0 with BSA. The pH of the digested labeled peptide mixture was adjusted by adding 200 mM HEPES pH 7.0 to a final concentration of 20 mM. Beads were spun down again, the supernatant removed, and each sample was added to one tube of bead mixture followed by room temperature incubation in the dark with gentle rocking for overnight. The entire reaction was added to the top of the column and let it drain into a microcentrifuge tube. The reaction tube was washed with 50% Acetonitrile 50% 20 mM HEPES pH 7.0. Beads were washed by adding 1 mL of each solution in the following order: H_2O; 5 M NaCl; 50% Acetonitrile; 5% Formic Acid. 10 mM DTT was added to the column, allowing it to drain halfway, and then incubating for 10 minutes with the solution in the column. Then, a solution of 1 mg/mL Oxone pH ~3.5 in water was added to the column. Phospho-peptides were desalted and concentrated with a C-18 ziptip. Next, the ziptip was washed with 0.1% TFA 50% acetonitrile H_2O, then with 0.1% TFA H_20, then with 0.1% TFA H20 and eluted by washing with 0.1% TFA 50% Acetonitrile-H_2O. The sample was concentrated on a speed vacuum and analyzed by tandem mass spectrometry using a QSTAR ELITE that includes coupled liquid chromatography on a reverse phase C18 column utilizing a 3–32% acetonitrile gradient in 0.1% formic acid. MS spectra were acquired for 1s. For each MS spectrum the two most intense multiply charged peaks were selected for generation of subsequent collision-induced dissociation MS. The data was analyzed by centroiding using Analyst QS software. Search the MS/MS spectra against the entire UniProt database, selecting no constant modifications and allowing the following variable modifications: Phospho: Serine, Threonine, Oxidized: Methionine.

Purification of recombinant proteins

FER WT, FER AS, FER-D742R, MAPK1 and DCTN2/pGEX-6P-1 vectors were introduced into Rosetta bacteria, and transformants were plated on LB-agar plates containing ampicillin (Sigma-Aldrich). Protein expression was induced for 16h at 18°C by adding 0.2 mM Isopropyl β-D-1-thiogalactopyranoside (Sigma-Aldrich). After induction, bacteria pellets were lysed in lysis buffer containing 10 mM EGTA, 10 mM EDTA, 0.1% Tween 20, 250 mM NaCl, 5 mM DTT, 0.325 mg/mL lysosome, and protease inhibitors (CompleteTM; Roche Applied Science). Cells were sonicated and centrifuged at 38k relative centrifugal force for 30 min at 4°C. Supernatants were coupled to glutathione-Sepharose 4B beads (Amersham Biosciences) and proteins were eluted in buffer containing 100 mM Tris (pH 8.0), 30 mM reduced glutathione and 75 mM KCl.

Immunoprecipitation and *in vitro* kinase reactions

Immunoprecipitation of phospho-MAPK1/3 was performed as previously (van de Ven et al., 2015), using mouse anti-phospho-p44/42 MAPK (1:50; Cell Signaling, 9101s). MM231 DCTN2iKD expressing GFP-DCTN2^{WT} or GFP-DCTN2^{Y6A} were cultured in DOX-induced conditions (1 μg/mL, Sigma), for 10 days in 10cm dishes. GFP-Trap anti-GFP beads (#gta-20; Chromotek) were used to perform the co-immunoprecipitations.

Recombinant truncated FER kinases were included into a 25-μL reaction containing kinase buffer (10 mM MgCl2, 20 mM Tris buffer pH 7.5 and 0.1 mM Na_3VO_4 (SigmaAldrich)), Each reaction was supplemented with an equal amount (1 μL) of GST-Cortactin, GST-MAPK1 or GST-Tubulin (SRP5148, Sigma), ATPγS (250 μM, A 060-05, BioLog), N^6-furfuryl(Fu)-ATPγS (250 μM, F 008-05, BioLog), N^6-phenylethyl(Phe)-ATPγS (250 μM, P 026-05, BioLog) or N^6-benzyl(Bn)-ATPγS (250 μM, B 072-05, BioLog) with or without 10 μm NM-PP1 (Calbiochem). After 30 min at 30°C, the reactions were stopped using 0.5M EDTA. Thiophosphorylated samples were subsequently incubated with 2.5 mM *p*-nitrobenzyl mesylate (Epitomics, Burlingame, CA). After 2h at room temperature, 25 μL of 2× sample buffer was added to stop the reaction.

Immunoblotting analysis

MM231 cells were directly lysed in sample buffer, separated by SDS/PAGE and blotted. The following antibodies were used for immunoblotting analysis: mouse anti-FER (1:1000; Cell Signaling, 4268s), rabbit anti-GAPDH (1:1000; Millipore, Mab374); mouse anti-GST (1:1000; Santa Cruz, sc-138), mouse anti-thiophosphate ester (1:5000; Abcam, ab92570), rabbit anti-V5 (1:1000, 13202, Cell Signaling), rabbit anti-phospho-p44/42 MAPK (1:1000; Cell Signaling, 9101s), rabbit anti-phospho-p44/42 MAPK (1:1000; Cell Signaling, 4370s), mouse anti-p44/42 MAPK (1:1000, Cell Signaling, 9107), mouse anti-phospho tyrosine (1:500; BD Transduction, 610000), mouse anti-DCTN2 (1:500; Santa Cruz, sc-393389). Detection was performed by using HRP-conjugated goat anti-mouse or goat anti-rabbit antibodies (1:5000; Bio-rad, 170-6516 or 170-6515) and Enhanced Chemi-Luminescence (ECL) detection (GE Healthcare). Detection was also performed using IRDy680 and IRDye800 labeled goat anti-rabbit or goat anti-mouse antibodies (1:5000; Li-Cor,926-68071 or 92632210). Quantification was done using the Image Studio Lite software (LI-COR Biotechnology).

Immunofluorescence analysis

Specimens for immunofluorescence (IF) microscopy were prepared as described (Tavares et al., 2017). Briefly, cells were plated in glass coverslips and fixed in 4% paraformaldehyde in PBS at pH 7 for 20 min and permeabilized with TBS-T (TBS—0.1% Triton X-100) at room temperature. Cells were blocked in PBS-T supplemented with 10% BSA for 1 h at room temperature. Primary antibodies were incubated overnight at 4°C in blocking solution. Coverslips were then washed three times with PBS and incubated

with secondary antibodies and with Rhodamine-conjugated Phalloidin (Sigma, P-1951) at 0.3 mM in blocking solution for 1 h at room temperature. After three washes in PBS, cells were stained with 2 μg/mL DAPI (Sigma, D9542) for 5 min. in TBS, washed again with PBS and mounted on Prolong. Confocal analysis was conducted with a Plan-Apochromat 63× /1.40 Oil DIC M27 or with a LD Plan-Neofluar 40x/0.6 Korr M27 objectives mounted on an inverted Carl Zeiss LSM 700 Laser Scanning Microscope. For immunofluorescence staining of αTubulin (tyrosinated /detyrosinated) and CAMSAP-2, cells were fixed in cold methanol for 10 min at -20 ºC. Imaging was performed using a Nikon Eclipse Ni-U Microscope, Ni 100x NA 1.45 oil immersion objective. Images were acquired and analyzed with ImageJ software.

Primary antibodies used: anti-phospho Paxillin (1:100; Life Technologies, 447226), mouse anti-αTubulin (1:1000; #T5168, Sigma-Aldrich), mouse anti-LAMP1 (1:500; MA1-164, Thermo Fisher Scientific), rat anti-β1 Integrin (1:200, 528306, Developmental Studies Hybridoma Bank), rat anti-α6 Integrin (Sonnenberg et al., 1987) (1:20), mouse anti-Rab4b (1:50, 271982, Santa Cruz Biotechnology), rabbit anti-Rab11(1:200, 71-5300, Thermofisher), rabbit anti-EEA1 (1:100, 3288, Cell Signaling Technology), rabbit anti-DCTN2 (1:100, HPA039715, Sigma Aldrich) and Ki-67 (1:50, M7240, Dako), rat anti-tyrosinated α-tubulin (1:200; MA1-80017, Thermo Fisher Scientific), rabbit anti-de-tyrosinated αTubulin (1:200; ab48389, Abcam) and rabbit anti-CAMSAP2 (1:200; NBP1-21402, Novus). Secondary antibodies used were: Alexa-488-, Alexa-594, Alexa-647, Alexa-633, and Alexa-568-conjugated goat antibodies against rat, rabbit and mouse (1:200; all from Molecular Probes by Invitrogen).

Live cell imaging

MM231 FER iKD or DCTN2 iKD cells were induced for 5 days with or without Dox, and MM231 FER^{RECON} cells were treated for 3 days with NM-PP1 or DMSO (control), before plating them on 8-well glass-bottom plates (Ibidi, Gräfelfing, Germany). Cells were imaged every 15 min. for 16 h. using a Olympus Cell-M imaging system with an UPlanFL N 20x/0.50 objective. During imaging, cells were kept in complete DMEM medium (with or without DOX, or with DMSO or NM-PP1) under normal growth conditions (37°C, 5% CO2). Cell migration was quantified using the Imaris for Tracking software (Bitplane, Oxford Instruments, UK) or TrackMate (Tinevez et al., 2017) plugins.

Cell were treated with 200nM SiR-Lysosome (Tebu-bio, SC012) 1hr before imaging. Fluorescence imaging of live cultures was performed on a Nikon spinning disk-based confocal imaging station with the Perfect Focus System equipped with Plan Apo VC 100x N.A. 1.40 oil objective. Imaging of lysosomes with SiR-Lysosome was performed at 0.05 s for 600s. The length of the directional tracks was analyzed using the MTrackJ plugin for vesicle tracking.

BSA/Transferrin uptake assay

Cells were incubated for 3hrs in medium with BSA-Alexa555 (10 ug/mL; A34786, Invitrogen). For Transferrin uptake studies, cells were first incubated on ice for 10 min, then Transferrin-Alexa647 (50 μg/mL; T23366, Invitrogen) was added and incubated for 15 min. Cells were rinsed with PBS and fixed with 4% PFA for 2hr at RT. Samples then followed the same immunofluorescence protocol described above. Samples were imaged on a DeltaVision widefield microscope using a×100/1.4 A immersion objective. Pictures were deconvolved using Softworx software and analyzed using Fiji ImageJ v1.48q (Schneider et al., 2012). Quantification of colocalization was done using Volocity high-performance image analysis software (Quorum Technologies) or with Comdet plugin in FiJi (https://github.com/ekatrukha/ComDet).

Cell counting and cell cycle profiling

Cell numbers were quantified using the Countess™ Cell Counter (Invitrogen) and fixed in 70% ethanol. Cells were washed and incubated with staining solution containing 20 μg/mL propidium iodide and RNase 100 μg/mL and analyzed by flow cytometry (FACSCelesta; BD Sciences). FlowJo, LLC software was used for quantification of the percentage of S-phase cells. Quantifications are from at least three biological replicates.

Colony formation assays

Optimal drug concentrations were determined by serial dilution for each cell line. Cells were treated with docetaxel (Accord, India) or Paclitaxel (BML-T140, Enzo Life Sciences) for three days within a range of 0.1 nM – 250 nM and with DMSO as vehicle control. Experiments were performed at least three times. Cells were fixed with media containing 2.5% glutaraldehyde (Sigma) for 10 min and stained with 0.1% Crystal Violet (Sigma) for 30 min. Proliferation rate/crystal violet intensity was determined by washing the cells for 30 min with 10% acetic acid and measuring optical density (OD) at λ=595nm. IC50 values and significance were calculated using four parameters logistical regression, non-linear fit of exponential decay test and unpaired two-tailed Student's multiple t-test, respectively.

Clinical data analyses

RNA seq datasets from the MATADOR study (Dutch Breast Cancer Research Group (BOOG) BOOG 2005-02) (van Rossum et al., 2018) were obtained from formalin-fixed, paraffin-embedded primary tumor specimens (submitted to be published) and were used to study the association between FER mRNA expression levels and patient outcome after six adjuvant cycles of dose-dense doxorubicin and cyclophosphamide (ddAC) or six cycles of docetaxel, doxorubicin and cyclophosphamide (TAC) (van Rossum et al., 2018). For 574 patient tumor samples good quality RNA sequencing data could be obtained. Out of the normalized and log2

transformed data (with use of DESeq2) the FER expression per patient was measured. FER high was defined as an RNA expression above the median [8.538] value derived from FER expression levels measured in all patients. Correlation of FER expression with clinicopathological features of the patient cohort is presented in Table S4 and tested for difference in distribution using the Pearson Chi-square test (R version 3.6.1, package tableone 0.1.11).

Recurrence-free survival was defined as the interval between randomization and locoregional or distant relapse or death by any cause. We assessed whether the effect of adjuvant TAC versus ddAC chemotherapy on recurrence-free survival, expressed as the hazard ratio, differed by FER status based on multivariate proportional hazards regression with an interaction term, adjusting for the following potential confounders: Tumor size, lymph node status, histologic grade, age and type of surgery. Results of the model are reported with corresponding confidence intervals (CI) fitted for RFS, and interaction p-values (alpha 0.05). Recurrence-free survival was evaluated according to FER status by Kaplan–Meier curves and log-rank statistics (Packages survival 3.1.11, survminer 0.4.6).

QUANTIFICATION AND STATISTICAL ANALYSIS

Quantification of colocalization assays

ImageJ plugin Comdet v.0.3.61 (Katrukha, 2020) (https://github.com/ekatrukha/DoM_Utrecht) was used for detection and fitting of single molecule fluorescent spots. With this method, individual spots are detected in both channels and the percentage of the signal (pixels) that is shared between both channels is measured. Quantification was performed for 3 separate experiments with n>40 cells.

3D morphology quantification

Each image was segmented by individually optimizing the OrganoSeg (Borten et al., 2018) parameters manually until a suitable segmentation was achieved. Invasiveness was inferred using 'Solidity' parameter (*Invasiveness=1-Solidity*) reported in each spheroid caption.

Analysis of live cell imaging data

Cell migration was quantified using the Imaris for Tracking software (Bitplane, Oxford Instruments, UK) or TrackMate (Tinevez et al., 2017) plugins.

Imaging of lysosomes with SiR-Lysosome was performed at 0.05 s for 600s. The length of the directional tracks was analyzed using the MTrackJ plugin for vesicle tracking.

Quantification of immunofluorescence

Ki67 and phospho-Paxillin

For each experiment, all images were acquired with identical illumination settings. Image analysis was performed with Fiji image processing software (ImageJ). Immunofluorescence images were quantified for both phospho-Paxilin (pPax) and Ki67 signal using macros in FIJI. For pPax quantification, Phalloidin signal was used to demarcate cells via thresholding and nuclei were demarcated using DAPI signal and ''Analyze particles'', excluding nuclei that were cut off by the image border. Subsequently, pPax foci were quantified using ''Find Maxima'' command in conjunction, after which foci were measured within the demarcated cells. Finally, in Excel, pPax data was converted from signal to foci and number of foci was averaged to the number of cells quantified in the image, determined by number of nuclei. Significant differences between conditions were visualized and tested in Graphpad Prism 9 software.

For Ki67 quantifications, DAPI was used to demarcate the nuclei, after a smooth and ''Gaussian blur'' to increase definition of nuclei in spheroids. Nuclear ROIs were established after thresholding with the DAPI signal and using ''Analyze particles'' command. Finally, Ki67 signal was measured within these ROIs and exported to Excel. Per image, nuclear ROIs were filtered based on size ($25 \geq ROI \leq 250$) to exclude debris and merged ROIs. Afterwards, Ki67 thresholds were established image by image, using the average of the five lowest Integrated Densities multiplied by three, accounting for signal intensity differences due to imaging depth in gels. Significant differences between conditions were visualized and tested in Graphpad Prism 9 software.

Quantifications of Rab4- and Rab11-positive vesicle areas

Size analysis of Rab4 and Rab11 positive endosomal organelles was done using the Comdet plugin in Fiji (https://github.com/ekatrukha/ComDet) (Schindelin et al., 2012) First, cellular areas in the images (2 or 3 per image) were selected and identified as region of interest (ROI) using the actin labelling (Phallodin-Alexa^{488}) signal in the images. Objects were subsequently detected with the ComDet plugin of Fiji in the respective Rab4 or Rab11 channels. Values of 'NArea' were chosen to measure Rab4 and Rab11 objects with puncta and tubule-like appearances. 10 images (20-30 cells) from 3 independent experiments were processed. Area of Rab4 and Rab11 particles were obtained from the output table from the ComDet plugin, averaged per image, and plotted in GraphPad.

Mass spectrometry

Raw mass spectrometry data were processed using MaxQuant version 1.5.1.6, with an false-discovery rater (FDR) < 0.01 at the level of proteins, peptides and modifications, using default settings with the following minor changes: oxidized methionine (M), acetylation (protein N-term) and phospho (STY) were selected as variable modifications, and carbamidomethyl (C) as fixed modifications minimum peptide length of six amino acids, and ''match between runs'' (MBR) was enabled with a matching time window of

1 min. Proteins and peptides were identified using a target-decoy approach with a reversed database, using the Andromeda search engine integrated into the MaxQuant environment. Searches were performed against the Human UniProt FASTA database quantification of peptides and proteins was performed by MaxQuant. Bioinformatics analysis was performed with Perseus, Microsoft Excel and R statistical computing software. Annotations were extracted from UniProtKB, Gene Ontology (GO), Kyoto Encyclopedia of Genes and Genomes (KEGG), Reactome, Ingenuity IPA and NCI-Nature. Significance was assessed by Student's t-test, using permutation-based FDR to control for multiple hypothesis testing.

Statistical analysis

Statistical significance was analyzed either using the Mann-Whitney U test, or t test, as indicated in the figure legends. For the t tests, data distribution was checked for normal distribution of the data. Error bars represent the standard deviation (SD). The asterisks indicate significant differences. Statistical analysis was performed with Graphpad Prism 9 software.